Dynamic Normalization

David J. Heeger*[,1,2] and Klavdia O. Zemlianova[2]

Department of Psychology[1] and Center for Neural Science[2]
New York University
4 Washington Place, room 923
New York, NY 10003

*: Corresponding author
Email: david.heeger@nyu.edu
ORCID ID: 0000-0002-3282-9898

Classification. Biological Sciences: Neuroscience; Social Sciences: Psychological and Cognitive Sciences.

Keywords: computational neuroscience, recurrent neural network, V1, normalization, gamma oscillation

Abstract

The normalization model has been applied to explain neural activity in diverse neural systems including primary visual cortex (V1). The model's defining characteristic is that the response of each neuron is divided by a factor that includes a weighted sum of activity of a pool of neurons. In spite of the success of the normalization model, there are 3 unresolved issues. 1) Experimental evidence suggests that normalization in V1 operates via recurrent amplification, i.e., amplifying weak inputs more than strong inputs. It is unknown how normalization arises from recurrent amplification. 2) Experiments have demonstrated that normalization is weighted such each weight specifies how one neuron contributes to another's normalization pool. It is unknown how weighted normalization arises from a recurrent circuit. 3) Neural activity in V1 exhibits complex dynamics, including gamma oscillations, linked to normalization. It is unknown how these dynamics emerge from normalization. Here, a new family of recurrent circuit models is reported, each of which comprises coupled neural integrators to implement normalization via recurrent amplification with arbitrary normalization weights, some of which can recapitulate key experimental observations of the dynamics of neural activity in V1.

Significance Statement

A family of recurrent circuit models is proposed to explain the dynamics of neural activity in primary visual cortex (V1). Each of the models in this family exhibits steady state output responses that are already known to fit a wide range of experimental data from diverse neural systems. These models can recapitulate the complex dynamics of V1 activity, including oscillations (so-called gamma oscillations, ~30-80 Hz). This theoretical framework also explains key aspects of working memory and motor control. Consequently, the same circuit architecture is applicable to a variety of neural systems, and V1 can be used as a model system for understanding the neural computations in many brain areas.

Introduction

The normalization model (1, 2) was initially developed to explain stimulus-evoked responses of neurons in primary visual cortex (V1) (1-6), but has since been applied to explain neural activity and behaavior in diverse cognitive processes and neural systems (7-47). The model's defining characteristic is that the response of each neuron is divided by a factor that includes a weighted sum of activity of a pool of neurons (**Fig. 1a**). The normalization weights specify the contribution of one neuron to another's normalization pool. In V1, this normalization pool includes neurons selective for different visual stimulus features and spatial positions (i.e., receptive-field locations). The model predicts and explains many well-documented physiological phenomena in V1 including response saturation, cross-orientation suppression, and surround suppression (**Fig. 1b, c**) (25, 48-58), and their perceptual analogues (59-63). For most visual neurons, responses to two or more stimuli presented together are much less than the linear sum of the individual responses. But different stimuli suppress responses by different amounts (12, 50, 55, 56, 64-67), suggesting the normalization is "tuned" or "weighted". The normalization weights mentioned above specify the tuning of normalization.

Neural activity in V1 exhibits complex dynamics, linked to normalization. The rate of response increase following stimulus onset is different from the rate of response decrease following stimulus offset (68). The rate of response increase is also stimulus dependent, and is faster for stimuli placed in the center of a receptive field (RF) and slower on the flanks of the RF (68). The timing of response suppression depends on its strength (67). Temporal-frequency tuning depends on stimulus contrast, and simple cell response phase depends on contrast (6, 50, 69-71). Complex dynamics are evident also in the combined activity (e.g., as measured with local field potentials, LFPs) of populations of neurons. LFPs exhibit so-called gamma oscillations (~30-80 Hz) that have also been linked to normalization (31, 72). Oscillation amplitude and frequency depend systematically on stimulus contrast, size, and spatial pattern (31, 72-86).

The circuit mechanisms underlying normalization are not well understood. Experimental evidence suggests that normalization operates via recurrent amplification, i.e., amplifying weak inputs more than strong inputs (39, 87-90). The recurrent amplification idea is supported by anatomy: cortical circuits are dominated by recurrent connections (91-96). We have known since we first introduced the normalization model that it can be implemented in a recurrent circuit (1, 5). Since then, several hypotheses for the recurrent circuits underlying normalization have been proposed, including shunting inhibition, synaptic depression, and inhibition-stabilized networks (6, 35, 50, 97-101). But these models do not rely on recurrent amplification to achieve normalization, they only approximate weighted normalization, and/or they do not exhibit complex dynamics (including gamma oscillations) linked to normalization.

Here, we introduce and characterize a family of dynamical systems that implement normalization with recurrent amplification. When the input drive is constant over time, each of the recurrent circuits in this family may achieve a fixed point in which the output responses follow the normalization equation exactly, with arbitrary (non-negative) normalization weights. Each model in this family is expressed as a coupled system of neural integrators, composed of two classes of neurons: principal neurons and modulator neurons. The key idea is that the amount of recurrent amplification in the principal neurons depends inversely on the responses of the modulator neurons. When the input is weak, the modulator neurons have small responses and there is a large amount of recurrent amplification. When the input stimulus is strong, the modulator responses are large, which shuts down the recurrent amplification. The various models in this family of dynamical systems imply different circuits, some (but not all) of which recapitulate the complex dynamics V1 activity, including gamma oscillations.

MATLAB code for recreating the simulation results is available at http://hdl.handle.net/2451/61045 (102).

Results

Recurrent normalization

Following our previous work (103-105), responses of a population of V1 neurons are modeled as dynamical processes that evolve over time in a recurrent circuit (**Fig. 2**). The time-varying firing rates of a population of V1 simple cells y_j depend on the sum of an input drive (**Fig. 2**, blue) and a recurrent drive (**Fig. 2**, green). The input drive is a weighted sum of the responses x_k of a population of neurons

in the lateral geniculate nucleus (LGN) of the thalamus. The LGN cells, in turn, receive their inputs from neurons in the retina that respond to visual stimulation (**Fig. 2**, thick horizontal bar). The recurrent drive is modulated by the responses of two populations of modulator neurons: a_j and u_j. (We use the term "modulator" to mean a multiplicative computation regardless of whether or not it is implemented with neuromodulators). The responses of the modulators depend on the simple-cell responses (**Fig. 2**, purple).

So there are two nested recurrent loops. 1) Recurrent amplification: simple-cell responses depend on the recurrent drive, which is a weighted sum of their own responses (**Fig. 2**, green). 2) Multiplicative modulators: the recurrent drive is modulated (multiplicatively) by the responses of the modulator neurons, and the modulator responses depend on a sum of simple-cell responses (**Fig. 2**, purple). The modulators control the amount of recurrent amplification. Increasing the simple-cell responses causes the modulator responses to increase which causes the amount of recurrent amplification to decrease. These two recurrent loops oppose each other such that the activity of the circuit may achieve a fixed point at which the neural activity is normalized. If the modulators are sluggish then the responses can exhibit an initial transient overshoot before achieving the fixed point. If instead the modulators have a short time constant and a delay, then the fixed point may be unstable and the responses may exhibit oscillations.

The end result is that the steady-state responses of simulated simple-cell behave like spatiotemporal linear filters with various orientation preferences and temporal phases, that are half-squared (halfwave rectified and squared) (106) and normalized (1, 2). V1 complex-cell responses are simulated by summing simple-cell responses with different temporal phases. Consequently, the steady-state responses of complex cells behave like normalized, spatiotemporal 'energy' filters, so-called because the responses depend on the local spectral energy (ignoring phase) in a local spatiotemporal window of the stimulus (106, 107). But for some stimulus conditions, the simulated responses fail to achieve steady state, and instead exhibit oscillatory responses.

Specifically, neural responses are modeled by the following dynamical systems equations:

$$\tau_v \frac{dv_j}{dt} = -v_j + \left(\tfrac{b_0}{1+b_0}\right) z_j + \left(\tfrac{1}{1+a_j}\right) \hat{y}_j \ , \qquad (1)$$

$$y_j = \lfloor v_j \rfloor^2 \ ,$$

$$\mathbf{z} = \mathbf{W}_{zx}\mathbf{x} \ ,$$

$$\hat{\mathbf{y}} = \mathbf{W}_{\hat{y}y}\sqrt{\mathbf{y}} \ ,$$

$$\tau_a \frac{da_j}{dt} = -a_j + \sqrt{u_j} + \sqrt{u_j}\, a_j \ , \qquad (2)$$

$$\tau_u \frac{du_j}{dt} = -u_j + \sum_k w_{jk} y_k u_k + \left(\tfrac{\sigma b_0}{1+b_0}\right)^2 \ . \qquad (3)$$

The variables ($\mathbf{y}$, $\mathbf{v}$, $\hat{\mathbf{y}}$, $\mathbf{x}$, $\mathbf{z}$, $\mathbf{a}$, $\mathbf{u}$) are each functions time, e.g., $\mathbf{y}(t)$, but we drop the explicit dependence on t to simplify the notation. Vector $\mathbf{y} = (y_1, y_2, \ldots, y_j, \ldots, y_N)$ represents the firing rate responses of simple-cells, where the subscript j indexes different neurons in the population, with different RF centers, orientation preferences, and temporal phases. (Boldface lowercase letters denote vectors and boldface uppercase letters denote matrices.) The underlying membrane potentials of the simple cells are represented by vector $\mathbf{v}$. Membrane potential is half-squared to yield the firing rates (**Eq. 1**, 2nd line). Vector $\mathbf{x} = (x_1, x_2, \ldots, x_k, \ldots, x_M)$ represents the time-varying firing rates of the LGN inputs. Vectors $\mathbf{a}$ and $\mathbf{u}$ represent responses of the two types of modulator neurons. Vector $\mathbf{z}$ is the input drive and $\hat{\mathbf{y}}$ is the recurrent drive. The values of τ_v, τ_a, and τ_u are intrinsic time constants of the corresponding cell classes, b_0 is a constant that determines in the input gain, and σ is a constant that determines the contrast gain of the responses (see below). The input drive z_j (**Eq. 1**, 3rd line) is a weighted sum of LGN inputs x_k (**Fig. 2**, blue; see *SI Appendix* for details). The rows of the weight matrix $\mathbf{W}_{zx}$ determine the spatial RFs of the simple cells (**Figs. S1b**,**c**,**d**; see *SI Appendix* for details). The recurrent drive $\hat{y}_j$ (**Eq. 1**, 4th line) is a

weighted sum (with recurrent weights $\mathbf{W}_{\hat{y}y}$) of the square-root of the responses y_j (**Fig. 2**, green; see *SI Appendix* for details). The recurrent drive is modulated by one population of modulators a_j (**Eq. 1**, last term), which in turn depend on the other population of modulators u_j (**Eq. 2**). The modulators u_j depend on the simple-cell responses y_j (**Fig. 2**, purple; **Eq. 3**).

When the input drive is constant over time, the circuit can achieve a fixed point in which the neural activity is normalized:

$$\mathbf{y} = \frac{\lfloor \mathbf{z} \rfloor^2}{\sigma^2 + \mathbf{W}\mathbf{z}^2} \ , \qquad (4)$$

where the numerator is half-squared, and the quotient means element-by-element division. To derive **Eq. 4**, set the derivatives in **Eqs. 1-3** equal to 0 and simplify (see *SI Appendix*). The values of w_{jk} in **Eq. 3** are the normalization weights, i.e., the elements of $\mathbf{W}$ in **Eq. 4**. Variants of **Eq. 4** (with various exponents) have been fit to a wide range of experimental data (1-67).

Recurrent normalization, as implemented in Eqs. 1-3, agrees with experimental results demonstrating that normalization operates via recurrent amplification i.e., amplifying weak inputs more than strong inputs (39, 87-90). The recurrent drive involves both excitation and inhibition (**Fig. 2**, green solid and dashed lines, respectively). The modulators control the amount of recurrent amplification (**Fig. 2**, purple line with circle head). Consequently, both excitatory and inhibitory recurrent signals (**Fig. 2**, green) are amplified by an amount that is controlled by the modulators (**Fig. 2**, purple).

Furthermore, we can derive expressions for the effective gain and the effective time constant of the responses, to generate experimentally-testable predictions and for fitting data. The effective gain and effective time constant both depend on the input stimulus. Weak stimuli are strongly amplified (large effective gain) via the recurrent circuit which takes a period of time (long effective time constant). Strong stimuli are weakly amplified (small effective gain) which happens more quickly (short effective time constant). The effective gain of each neuron in the circuit (the ratio of each element of $\mathbf{y}$ to each element of $\mathbf{z}^2$) depends on the input drive and the normalization weights: $\mathbf{W}\mathbf{z}^2$ (**Eq. 4**). The effective time constant depends on the effective gain (see *SI Appendix*) so it too depends on $\mathbf{W}\mathbf{z}^2$. For stimuli comprised of sinusoidal gratings or pairs of gratings:

$$r \propto \frac{c_t^2}{\sigma^2 + c_t^2 + \beta c_m^2} \ , \qquad (5)$$

$$g = \frac{1}{\sigma^2 + c_t^2 + \beta c_m^2} \ , \qquad (6)$$

$$\tau = \tau_v \left(\frac{1+b_0}{b_0} \right) \sqrt{g} \ , \qquad (7)$$

where r is the amplitude of modulation of a simple cell's response (or the mean firing rate of a complex cell), g is the effective gain of that neuron's responses, and τ is that neuron's effective time constant (see *SI Appendix*). The value of c_t is the contrast of a test grating (e.g., a preferred orientation grating restricted to the RF). The value of c_m is the contrast of a mask grating that by itself does not evoke a response. The value of $0<\beta<1$ depends on the normalization weights. From **Eq. 5**, it is evident that responses saturate (level off) when the test contrast is large ($\gg\sigma$), cross-orientation suppression results when a mask grating is superimposed that is orthogonal to the preferred orientation, and surround suppression results when a mask grating is added in the region surrounding the RF, all characteristics of visual neurophysiology (**Fig. 1**). From **Eqs. 6-7**, it is evident that these stimulus components also have an impact on the timing of the responses.

The circuit model expressed by **Eqs. 1-3** is but one example of a family of dynamical systems models of normalization, each of which implements normalization via recurrent amplification (see *SI Appendix*). Some of these various models exhibit qualitatively different dynamics (see *SI Appendix*). For example, one of these variants has a single type of modulator instead of two, but it can be ruled out as a plausible model of V1 activity because it does not exhibit dynamics commensurate with V1 activity (see *Variants of the model*).

Simulated neural responses in the following figures are intended to exhibit qualitative aspects of neurophysiological phenomena, i.e., the models have not (yet) been optimized to replicate published data by tuning or fitting the model parameters (see *SI Appendix*). Unless otherwise stated, model parameters were: b_0=0.2, σ=0.1, τ_v=1 ms, τ_a=2 ms, τ_u=1 ms. The LGN inputs had 2 temporal impulse response functions (**Fig. S1a**, see *SI Appendix*), with quadrature phases, matching the preferred temporal frequency of the cortical cells (ω=8 Hz, see *SI Appendix*). There were 12 orientation tuning curves (**Fig. S1b**, see *SI Appendix*) that evenly tiled orientation, i.e., the sum of the squares of the tuning curves was equal to 1 (**Fig. S1b**). The spatial RFs covered the visual field from -60° to 60° eccentricity, and tiled the visual field so that the sum of the squares of the RFs was equal to 1 (**Fig. S1c**, see *SI Appendix*). RF size increased with eccentricity (**Figs. S1d**, see *SI Appendix*), approximating measurements of V1 RF size and cortical magnification (108-112). The normalization pool included all orientations (evenly weighted) within a neuron's RF, but included only orientations near the preferred orientation for spatial locations surrounding the RF. The spatial size of the normalization pool was about 4x larger than the RF (**Fig. S1e**), except where it was limited in size near the edge of the field of view (near ±60° eccentricity). The normalization weight matrix $\mathbf{W}$ was scaled such that the effective gain was g=1 for a full-contrast, full-field grating with a neuron's preferred spatiotemporal frequency and orientation.

Recurrent amplification, effective time constant, onset transients, and oscillations

The recurrent circuit model (expressed by **Eqs. 1-3** and depicted in **Fig. 2**) mimics many features of the dynamics of V1 activity. We focus on response dynamics because the mean firing rates are given by **Eqs. 4-5** which are already known to fit a wide range of experimental data (**Fig. 1**) (e.g., 2, 6, 25, 50-52, 55, 56, 58).

Simulated responses to grating stimuli with various contrasts replicated experimental observations (**Fig. 3**). Response amplitudes of simulated simple- and complex-cells were exactly equal to **Eq. 5**, saturating at high contrasts (**Figs. 3a**,**e**,**f**). The modulator responses increased monotonically with contrast but did not saturate (**Fig. 3b**). Responses were amplified by 100x when contrast was low but by only ~1x when contrast was high (**Fig. 3c**), following **Eq. 6**. The effective time constant was correspondingly long for low contrasts but short for high contrasts (**Fig. 3d**), following **Eq. 7**. Consequently, high-contrast stimuli evoked rapid increases in activity, whereas low-contrast stimuli evoked much slower and more gradual increases in activity before achieving steady state (**Fig. 3e**). The rate at which activity decreased following stimulus offset was different from the rate at which activity increased after lifting off from zero following stimulus onset (**Fig. 3e**). These results are similar to a variety of electrophysiological measurements (50, 58, 84, 113-118).

By changing one of the model parameters (specifically, the intrinsic time constant of the modulator neurons u_j), simulated responses to high contrast stimuli exhibited either strong transients following stimulus onset (**Fig. 3e**, τ_u=10 ms) or stable, high-frequency (~40-50 Hz) oscillations (**Fig. 3f**, τ_u=1 ms). Both of these phenomena – onset transients (115, 119, 120) and stable oscillations (31, 72-86) – have been widely reported from experimental observations.

In these simulations, the normalizations weights were all equal, so the response transients and/or oscillations were synchronized across the population of neurons. Consequently, in spite of the complex dynamics, ratios of the responses across neurons with different orientation preferences were maintained throughout each stimulus presentation, resembling some experimental results (115), and enabling an accurate readout of the stimulus orientation at any time point. With unequal (non-negative) normalization weights, response ratios evolved over time with non-stationary readout, analogous to other experimental results (121). Furthermore, with unequal normalization weights, response ratios also depended on stimulus contrast so that the simulated neural responses did not exhibit perfectly contrast-invariant tuning curves.

Disabling the recurrent amplification (i.e., simulating an experiment in which cortical spiking is shut down) attenuated the membrane potential response amplitudes by a factor of ~10x at high contrasts (**Fig. 3g**,**h**), while maintaining their orientation-selectivity, resembling electrophysiological results (122-125).

Temporal-frequency tuning and phase advance depend on contrast

Temporal-frequency tuning of both simple- and complex-cells depends on stimulus contrast, and

simple cell response phase depends on contrast (6, 50, 69-71). It was previously proposed that these phenomena can be explained by a recurrent normalization model in which a neuron's conductance (and consequently its intrinsic time constant) depends on stimulus contrast (6, 50). Here, we hypothesize instead that the effective time constant depends on contrast because the amount of recurrent amplification in the circuit decreases with increasing contrast (**Eqs. 6-7**).

Simulated temporal-frequency tuning depended systematically on contrast, responding to a broader range of temporal frequencies at high contrasts (**Fig. 4**). **Figs. 4a,b** plot results for ω=0 Hz, i.e., the recurrent drive in the model acted like a lowpass filter (see *SI Appendix*). Increasing stimulus contrast increased the responsivity of the simulated neurons for high temporal frequencies (see *SI Appendix*). **Figs. 4d,e** plot results for ω=8 Hz, i.e., the recurrent drive in the model acted like a bandpass filter, matching the preferred temporal frequency of the simulated LGN inputs. In this case, increasing stimulus contrast increased the responsivity of the simulated neurons for both low and high temporal frequencies. For low contrasts, temporal-frequency tuning was bandpass with a relatively narrow bandwidth. Increasing stimulus contrast transformed the temporal frequency tuning from bandpass to lowpass while nearly doubling the high temporal-frequency cutoff. This behavior arises in the model because the effective time constant depends on contrast: the effective gain decreases with increasing contrast (**Eq. 6**) and the effective time constant decreases with decreasing effective gain (**Eq. 7**). A shorter time constant corresponds to a broader bandwidth, raising the high temporal-frequency cutoff for a lowpass tuning curve, and raising both the low and high cutoffs for a bandpass tuning curve.

Response phase also depended systematically on contrast (**Figs. 4c,f**). For simulated simple cells with lowpass temporal-frequency tuning, response phases advanced with increasing contrast, more so for higher temporal frequencies (**Fig. 4c**). For simulations with bandpass temporal-frequency tuning, response phases shifted in opposite directions for temporal frequencies above and below the preferred temporal frequency (**Fig. 4f**).

Results like those shown in **Figs. 4a-c** have been observed experimentally (6, 50, 69-71): increasing phase advance and increasing the high temporal-frequency cutoff with increasing contrast. The model predicts that the effects shown in **Figs. 4d-f** may be evident for neurons with narrow temporal-frequency tuning, e.g., perhaps direction-selective neurons in layer 4b.

Response dynamics depend on stimulus location

The dynamics of V1 activity depends on whether a stimulus is placed in the center or flanks of a neuron's receptive field (68). Activity evoked by a small (< 1°) grating patch extends over a cortical region greater than 3x3 mm^2. Following stimulus onset, responses rise simultaneously over the entire active region, but reach their peak more rapidly at the center. Furthermore, the rate of response increase following stimulus onset is faster for higher contrasts. Following stimulus offset, responses fall simultaneously at all locations, and the rate of response decrease is the same for all locations and all contrasts. It was previously proposed that these phenomena can be explained by a recurrent normalization model in which a neuron's conductance (and consequently its intrinsic time constant) depends on the spatial distribution of stimulus contrasts, via the normalization weights (68). Here, we hypothesize instead that the effective time constant (as opposed to the intrinsic time constant) of each neuron depends on normalization weights.

Simulated responses recapitulated the experimentally-measured spatiotemporal dynamics (**Fig. 5**). Responses lifted off simultaneously following stimulus onset, but increased at a faster rate for RF locations centered on the stimulus (**Fig. 5**, darker colors), and for higher contrasts (**Fig. 5**, responses to 2nd stimulus presentation at t=500 ms). Recurrent amplification was weaker when the stimulus was presented closer to the center of a neuron's RF, and it was weaker for higher contrasts. Consequently, the effective gain was smaller (**Eq. 6**) and the time constant was shorter (**Eq. 7**) for these conditions. The effective time constant following stimulus offset was ~60 ms, regardless of what the stimulus had been (**Eqs. 6-7** with c_t=c_m=0, b_0=0.2, σ=0.1, and τ_v=1 ms).

Oscillations depend on stimulus contrast and size

Simulated responses exhibited oscillations at high frequencies that were induced (not evoked) by the stimuli (**Fig. 6**). For grating stimuli, these oscillations were evident only at high (> 50%) contrasts, and the oscillation amplitudes (**Fig. 6b**) and frequencies (**Fig. 6c**) both increased with stimulus size and

contrast. Response amplitudes, on the other hand, exhibited surround suppression so they were non-monotonic with stimulus size at high contrasts (**Fig. 6a**, dark gray and black curves). The oscillations depended indirectly on stimulus temporal frequency because the input drive to each neuron depended on stimulus temporal frequency with respect to the neurons' preferred temporal frequency (**Fig. 4**). That is, a lower contrast grating with a temporal frequency at the peak of the tuning curve induced the same oscillations as a higher contrast with a temporal frequency on the flank of the tuning curve, such that the two stimuli evoked the same input drive amplitudes. But the oscillations were otherwise (beyond the dependence on input drive amplitudes) independent of stimulus temporal frequency.

Oscillations were also evident for high contrast plaid stimuli, composed of a pair of orthogonal gratings, but the oscillations induced by plaids were smaller in amplitude and lower in frequency than those induced by gratings of the same contrast. Responses to plaids exhibited cross-orientation suppression; the response evoked by a 50% contrast grating with a neuron's preferred orientation was suppressed by about a factor of 2 when an orthogonal mask grating (also 50% contrast) was superimposed (**Fig. 6a**, dashed blue curve vs. 3rd to darkest gray curve). Oscillation amplitudes and frequencies induced by 100% contrast plaids were about midway between those induced by 50% contrast gratings and those induced by 100% contrast gratings (**Figs. 6b,c**, dashed blue curves).

The induced oscillations depended on the strength of the normalization pool, specifically, the product of the normalization weights and the input drive: $\mathbf{W}\mathbf{z}^2$. The normalization pool increased with contrast because the input drive $\mathbf{z}$ was proportional to contrast. The normalization pool increased with stimulus size because it comprised a weighted sum (with non-negative weights) over space. The normalization pool was smaller for a 100% contrast plaid then a 100% contrast grating. If the normalization was untuned such that all the normalization weights were 1, then the normalization pool for a 100% contrast plaid composed of two 50% contrast gratings ($\mathbf{W}\mathbf{z}^2 = 0.5^2 + 0.5^2$) would have been equal to that for a 70.7% contrast grating ($\mathbf{W}\mathbf{z}^2 = 0.707^2$). The simulated oscillations differed for these two stimulus conditions (**Figs. 6b,c**, dashed blue curve vs. 2nd to darkest gray curve) because the normalization pool included all orientations (evenly weighted) at the center of each neuron's RF, but only orientations near the preferred orientation for surrounding locations.

All of these results, except for one, are commensurate with experimental observations that oscillation amplitudes and frequencies depend systematically on stimulus contrast, size, and spatial pattern (31, 72-86), and that oscillations are linked to normalization (31, 72). Like the simulation results, oscillation amplitudes have been observed to increase with stimulus contrast and size, oscillation frequencies increase with stimulus contrast, and oscillations are smaller for plaids than for gratings (and even smaller for stimuli composed of multiple components, also predicted by the model). However, unlike the simulation results, oscillation frequencies have been reported decrease (instead of increasing) with stimulus size (31, 72, 82).

Phase space trajectories and bifurcation analysis

A bifurcation analysis was performed to fully characterize the induced oscillations over a wide range of parameter values (see *SI Appendix*). We analyzed a reduced version of the model in which each of the variables was a scalar instead of a vector (*SI Appendix*, **Eq. S37**), i.e., one neuron of each of the 3 types (y, a, and u) instead of a population of neurons with different RF centers and orientation preferences. We characterized the dynamics of the model as a function of the input drive (z), the intrinsic time constants of the modulators (τ_a and τ_u), and the input gain (b_0). In this reduced model, the input was a step at time t=0 and maintained a constant value thereafter.

The model exhibited distinct behaviors with boundaries (state transitions) between them (**Fig. 7**). When the input drive was small, the fixed point was stable (i.e., an attractor) and simulated responses (y) achieved steady state with no oscillations (**Fig. 7a**, green point; **Fig. 7b**). When the input drive was large, the fixed point was unstable with a stable limit cycle and responses exhibited stable oscillations (**Fig. 7a**, red point and dotted gray curves; **Fig. 7d**). For a middle range of input drive amplitudes, the fixed point was a spiral attractor and responses exhibited oscillations transiently before achieving steady state (**Fig. 7a**, yellow point; **Fig. 7c**). The steady state responses increased monotonically with input drive until the bifurcation, at which point the responses exhibited stable oscillations around the fixed point and no longer achieved a steady state (**Fig. 7a**, intersection of solid black, dashed black, and dotted gray curves).

The input drive that induced a bifurcation depended systematically on model parameters (**Figs. 7e**). Each panel of **Fig. 7e** depicts a 2D bifurcation diagram, i.e., a 2D slice through the space of model parameters. Each panel indicates the input drives for which bifurcations occurred (solid black curves) for different values of τ_u, and the different panels correspond to different values of τ_v and τ_a. Also indicated are the oscillation frequencies (gray scale) when the model exhibited stable oscillations or zero (white) otherwise.

Variants of the model

The dynamical system expressed by **Eqs. 1-3** is but one example of a family of circuit models of normalization, each of which implements normalization via recurrent amplification (see *SI Appendix*). Some of these various models exhibit qualitatively different dynamics such that measurements of the dynamics of neural activity in V1 may be used to distinguish between the alternatives. Each of the various models in this family imply different circuits, such that they may be distinguished experimentally using cell-type specific indicators.

For example, one of these variants can be ruled out as a plausible model of V1 activity because it does not exhibit dynamics commensurate with V1 activity. This variant (see *SI Appendix*, **Eq. S35**) is a simpler circuit with only two types of neurons, a principal neuron and a single type of modulator instead of two. The circuit has a stable fixed point such that the primary neurons achieve steady state responses given by the normalization equation (**Eqs. 4-5**). We have been able to prove mathematically, over a very broad range of parameter values, that the fixed point is stable over the full range of input drives. That is, there is no parameter regime in which the responses exhibit stable oscillations (see *SI Appendix*).

Discussion

We developed a family of circuit models of normalization based on recurrent amplification. Each of the models in this family exhibits output responses with a fixed point that follows the normalization equation (**Eqs. 4-5**) exactly, for arbitrary (non-negative) normalization weights. This fixed point (**Eqs. 4-5**) is already known to fit a wide range of experimental data (1-67). The fixed point is unstable and the circuit achieves a dynamic equilibrium (i.e., a limit cycle) for large, high-contrast stimuli, particularly for narrow band stimuli like sinusoidal gratings. Under these circumstances, the responses exhibit gamma oscillations (**Figs. 3**, **6**, and **7**). The oscillations are induced by the recurrent circuitry, depending on the strength of the normalization pool (the product of the normalization weights and the corresponding input drive), thereby explaining the experimental observations that gamma oscillations are linked to normalization (31, 72). Furthermore, this family of models mimics other experimental observations of V1 dynamics, linked to normalization, including the contrast dependence of the rate of response increase following stimulus onset and response decrease following stimulus offset (**Figs. 3** and **5**), and the contrast dependence of temporal-frequency tuning and phase advance (**Fig. 4**).

This family of recurrent circuit models, **O**scillatory **R**ecurrent **Ga**ted **N**eural **I**ntegrator **C**ircuit**s** (ORGaNICs), also explain key aspects of working memory and motor control (103-105). ORGaNICs are a generalization of and a biophysically-plausible implementation of Long Short Term Memory units (LSTMs) (126), a class of artificial recurrent neural networks, that have been applied to a number of machine learning applications including video summarization, language modeling, translation, and speech recognition. By virtue of being a generalization of LSTMs, ORGaNICs inherit all of the capabilities LTSMs. Consequently, the theoretical framework proposed here actually works – it is capable of performing useful computations that solve real-world problems. Furthermore, ORGaNICs can be used to explain the complex dynamics of delay-period activity during a working memory task, how information is manipulated (as well as maintained) during a delay period, and how that information is read out from the dynamically varying responses at any point in time in spite of the complex dynamics. When applied to motor systems, ORGaNICs can be used to convert spatial patterns of premotor activity to temporal profiles of motor control activity: different spatial patterns of premotor activity evoke different motor control dynamics. Here, we demonstrate that this same circuit architecture can simulate the dynamics of neural activity in V1. Consequently, this theoretical framework is applicable to diverse cognitive processes and neural systems, and we can use V1 as a model system for understanding the neural computations and circuits in many brain areas.

Gamma oscillations

Narrow-band gamma oscillations have been proposed to play a functional role in stimulus feature binding (127-130), attention (131-134), and/or synchronizing neuronal activity to enhance signal transmission and communication between brain areas (130, 133, 135-142). These speculations have been met with considerable skepticism (74, 77, 79, 82, 83, 143-147), in part because oscillation amplitude depends strongly on stimulus conditions (31, 72-86), incommensurate the perception of those stimulus conditions.

Gamma oscillations in the current family of models emerge from the nonlinear dynamics of the recurrent circuit. Synchronized spiking is not required to generate gamma oscillations and the model does not attribute any particular functional role to synchronization. Nor does the current model rule out the possibility that gamma oscillations serve to enhance signal transmission and communication.

The models exhibited gamma oscillations for a restricted subset of stimulus conditions, depending on the strength of the normalization pool. Consequently, oscillation amplitude was strongest for large, high contrast gratings, and weaker (or non-existent) for other spatial patterns and low contrasts, similar to experimental results (31, 72-86)

Long wavelength stimuli have been found to evoke particularly large amplitude gamma oscillations (85, 148). It should be straightforward to extend the current models to account for these results by including red-green and blue-yellow color-opponent channels (149-151) in the LGN input, and by setting the normalization weights to be large for the red-green channel.

The current theoretical framework is most similar to the so-called pyramidal-interneuron gamma (PING) mechanism for producing gamma oscillations, as opposed to the so-called interneuron gamma (ING) mechanism (146, 152-163). ING models generate oscillations with an interconnected network of inhibitory neurons (although some of these models rely on weak excitatory interconnections to synchronize the oscillations across multiple subpopulations of inhibitory neurons). In PING models, on the other hand, networks of excitatory and inhibitory neurons are reciprocally connected to generate oscillations. A volley of activity in the excitatory cells recruits a slightly delayed volley of activity in the inhibitory cells, which inhibits the excitatory cells for a gamma cycle, after which they recover. In line with PING models, we observed that the simulated activity of the modulators lagged (~90° phase) behind the activity of principal neurons when oscillations were induced.

Failures and extensions

Simulated oscillation frequencies increased with stimulus size (**Fig. 6**), unlike the experimental measurements that decreased with stimulus size (31, 72, 82). Previous models have tackled this problem by incorporating a mechanism that pools over large spatial regions that provides excitatory feedback to the principal neurons (82, 162). The current family of models may, likewise, be extended by enhancing the recurrent drive with an additional weighted sum a larger region of the visual field (105). We have verified that doing so may explain the observed decrease in oscillation frequency with increasing stimulus size. In addition, such recurrent spatial summation might explain various empirical measurements of contour integration (164-169).

Stable oscillations were induced in the simulation results for input drives (i.e., contrasts) above a threshold level (above the bifurcation), but narrow-band gamma power has been observed experimentally to change gradually with continuous parametric variation in stimulus parameters. Weaker inputs induced transient oscillations (spiral attractor dynamics, **Fig. 7**) after stimulus onset in our model simulations, and such transient oscillations could be confounded with stable oscillations in some experimental results. Such transient oscillations may be induced also following saccades. Furthermore, all the simulation results reported above were performed in the absence of noise. With noise added to the input, we observed stochastic resonance in the gamma frequency range even for weak inputs (below the bifurcation). This suggests that gamma-band activity may be induced by broadband noise in neural activity (146, 162), because the noise spectrum is shaped by recurrent normalization to exhibit a resonant peak in the gamma-frequency range.

The effective time constants of the principal neurons in our simulations ranged from ~6 ms to ~60 ms, which is within a reasonable range for *in vivo* cortical neurons, but the values of the intrinsic time constants (1-2 ms) were extremely short. It is unclear if these intrinsic time constant parameters can be

measured experimentally. These values correspond to the membrane time constants of isolated neurons (with no recurrent circuitry) but with conductances equal to those of V1 neurons in an awake animal. Even in the absence of visual stimulation, there is considerable background synaptic activity *in vivo* that increases the conductance by a factor of ~10x, thereby shortening membrane time constants from ~80 ms to ~7 ms (170).

Attention is associated with both increases in the gain of visually-evoked responses (e.g., 15, 17, 19) and increases in induced gamma oscillations (31, 131-134, 139, 144, 171-175). The constant input gain parameter b_0 may be replaced by a variable vector $\mathbf{b}$, in combination with normalization, to model the effects of attention on sensory responses. The elements of $\mathbf{b}$ determine the relative attentional gain for each neuron in the circuit (i.e., with different RF centers and different orientation preferences). Extending the model in this way would yield steady state output responses that are already known to fit experimental measurements of response gain changes with attention (19-23, 32, 34, 41, 44, 46). This change to the model would also affect the dynamics of the responses, and may explain the ostensible link between attention and gamma oscillations (31, 144).

Cross-orientation suppression is faster than surround suppression (58, 62). The current model may be extended to explain these results by incorporating an additional delay for contributions to the normalization pool from surrounding spatial locations. We hypothesize that a single computational process can explain both forms of suppression; it may very well be that different circuits and/or cell types are involved but that both contribute in the same way to the recurrent amplification computation (albeit with different time constants or delays)

The latency (delay) of response onset is stimulus dependent (176), and is generally longer than offset latency (116). The current family of models cannot, however, be falsified by measurements of response latencies. Latency (delay) is different from the effective time constant (sluggishness). Latency may depend mostly on precortical processing and action potential conduction delays. For the simulations reported here, we assumed a particular form for the precortical temporal filter and negligible conduction delays. But the precortical filter and conduction delays could be changed without sacrificing the core idea that normalization arises from recurrent amplification, as expressed by **Eq. 1-3**.

Mechanisms

We have presented a computational theory for what computations are performed by neural circuits in V1, not how they are implemented. But we can offer some speculation about the underlying mechanisms. The key idea is that normalization operates via recurrent amplification i.e., amplifying weak inputs more than strong inputs (39, 87-90), and that the modulators control the amount of recurrent amplification. The circuit expressed by **Eqs. 1-3** comprises an excitatory principal neuron (y_j, possibly layer 5 pyramidal cell), an inhibitory modulator (a_j, presumably one or more of the inhibitory interneuron cell types) that acts via shunting inhibition, and another excitatory cell type (u_j, possibly layer 2-3 pyramidal cell) that makes local recurrent connections. **Eq. 1** may be implemented with a simplified biophysical (equivalent electrical circuit) model of a pyramidal cell (103, 105). The input drive involves both feedforward excitation and feedforward inhibition (**Fig. 2**, blue solid and dashed lines, respectively). The recurrent drive also involves both excitation and inhibition (**Fig. 2**, green solid and dashed lines, respectively), presumably via lateral connections within V1. These excitatory and inhibitory recurrent signals are both amplified by an amount that is controlled by the modulators. This is consistent with the experimental observation that surround suppression involves a decrease in both recurrent excitatory and recurrent inhibitory conductances (98). If the modulators are implemented with shunting, then that would predict a modest increase in inhibitory conductance (**Fig. 2**, purple modulatory input with circle head) as well, in addition to the decrease in recurrent inhibition (**Fig. 2**, green dashed line), possibly explaining why the observed decrease in excitation is greater than the observed decrease in inhibition (98). The squaring nonlinearity (**Eq. 1**, 2nd line) may be approximated with a high threshold in combination with neural noise (177-179). The square roots in **Eqs. 1** and **3** may be approimated by a saturating nonlinearity or replaced by adding another cell type to the circuit (see *SI Appendix*, **Eq. S39**). The modulators a_j may act via shunting inhibition (103, 105), although other mechanisms for multiplying neural signals may be substituted. The modulators may be implemented by V1 parvalbumin-expressing (PV) inhibitory interneurons (180) and/or somatostatin-expressing (SOM) inhibitory neurons (181) and/or loops through higher visual cortical areas (182-185) and/or thalamocortical loops (186-193). The modulator neurons are expected to have large RFs and broad orientation-selectivity (reflecting properties of the

normalization pool), consistent with the response properties of SOM and PV neurons, respectively. The normalization weights are expressed in **Eq. 3** as a summation over $w_{jk}\, y_k\, u_k$, each term of which may be computed in separate compartments of the dendritic tree of an individual neuron.

Some of the effects of cross-orientation suppression may be due to feedforward (not recurrent) mechanisms. Contrast saturation and rectification in LGN relay cells can largely account for the response suppression measured in cat primary visual cortex (194), and the responses of V1 neurons are suppressed by high temporal frequency stimuli that do not drive cortical responses (195). Consequently, cross-orientation suppression has been attributed to either precortical mechanisms (194), synaptic depression at the thalamocortical synapse (97), or fast feedforward inhibition via local interneurons within V1 (195), whereas feedback from higher visual cortical areas has been implicated in surround suppression (182-185). Nevertheless, few studies have addressed this question in macaque (58), and evidence suggests that cortical circuits make an important contribution to cross-orientation suppression (39). As noted in the preceding paragraph, thalamocortical loops may contribute to the computation of the modulators, along with lateral connections within V1 and feedback connections from higher visual cortical areas.

Comparison with previous models

The current theoretical framework is superior to both the original recurrent normalization model and alternative recurrent models of normalization (1, 5, 6, 35, 50, 97-101). First, none of the previous models converge exactly to the normalization equation (**Eqs. 4-5**) for arbitrary (non-negative) normalization weights. Although they may approximate weighted normalization, the extent to which the previous recurrent models fit the full range of experimental data is unknown. The current family of recurrent circuit models has a mathematically-tractable solution that equals weighted normalization. The mathematical tractability has practical consequences, enabling us to derive closed-form expressions (**Eqs. 4-7**; see also *SI Appendix*) for making experimentally-testable predictions and for fitting data. Second, the current theoretical framework, unlike previous models, mimics the dynamics of V1 activity, including induced gamma oscillations, linked to normalization, specifically for large, high-contrast, narrow-band stimuli. Third, most of the previous models do not rely on recurrent amplification to achieve normalization. Fourth, the current theoretical framework is applicable to diverse cognitive processes and neural systems (e.g., working memory and motor control), enabling us to use V1 as a model system for understanding the neural computations and circuits in many brain areas. Fifth, by virtue of being a generalization of LSTMs, the current theoretical framework can solve relatively sophisticated tasks.

The current family of models is similar in some respects to the inhibition stabilized network (ISN) (98) and the stabilized supralinear network (SSN) (100), but there are also crucial differences. All of these models include recurrent excitation that would be unstable if inhibition was absent or held fixed. All of them also include inhibitory stabilization, but the stabilizing inhibition in the current model is modulatory (multiplicative), unlike ISN and SSN in which inhibition is subtractive. Inhibitory stabilization, by itself, does not explain the phenomena associated with normalization. A linear recurrent model, that does not exhibit any of the nonlinear effects associated with normalization, may be stabilized by inhibition, i.e., such that it would be unstable if inhibition were removed or held fixed (100, 196). Normalization phenomena arise in the SSN model from a combination of amplification and inhibitory stabilization. SSN (100) and also earlier models (1, 5, 6, 50), amplify weak inputs more than strong inputs due to a power law relationship (e.g., half-squaring) between membrane depolarization and firing rate (106, 177-179). Removing the power function from SSN yields a linear model that is qualitatively different, in which the responses increase in proportion to contrast (100). The current family of models also includes half-squaring, but it is not critical for normalization. Removing the squaring yields qualitatively similar phenomena; for example, the contrast-response function would be proportional to $c/(c+\sigma)$ rather than $c^2/(c^2+\sigma^2)$. Instead normalization in the current models relies on recurrent amplification via the recurrent drive.

Predictions

The real value of this family of recurrent circuit models of normalization rests on whether it can push the field forward by making quantitative and testable predictions, leading to new experiments that may reveal novel phenomena. Some of these predictions are as follows.

- Our theoretical framework predicts a link between effective gain and effective time constant

(**Eq. 7**). This is analogous to the previous shunting inhibition model of normalization (6, 50), but the prediction of that model was that both the gain and time constant change with intrinsic conductance, whereas the effective gain and time constant in the current family of models is a network effect, controlled by the recurrent amplification in the circuit. This hypothesized link may be tested either electrophysiologically or using psychophysical/behavioral methods (62).

- The link between effective gain and effective time constant is further constrained by the value of the input gain b_0 (**Eq. 7**). The input gain of neurons in layer 4C (the input layer) may be estimated from intracellular measurements of membrane potential fluctuations with and without disabling cortical spikes (e.g., via optogenetics) as illustrated in **Figs. 3g,h**. The input gain may also be manipulated with attention (19-23, 32, 34, 41, 44, 46).

- We predict a link between the intrinsic time constants and oscillation frequencies (**Figs. 7e**). In our simulations, oscillation frequency depended systematically on the values of the intrinsic time constants (τ_v, τ_a, and τ_u), and the input gain (b_0). An experimental test of this prediction would involve manipulating the intrinsic time constant (i.e., the conductance) of a particular cell type in the circuit.

- The theory predicts that different stimulus conditions can evoke the same response amplitude and the timing, and induce the same oscillations. This will be the case for different stimuli that evoke the same input drive to a neuron and that have equivalent effects on that neuron's normalization pool. For example, consider a 50% contrast preferred-orientation target grating restricted to the RF center, superimposed with each of three different mask gratings: 1) an orthogonal grating restricted to the RF center, 2) a parallel grating restricted to the surround, and 3) an orthogonal grating restricted to the RF surround. Adjust each of the mask grating contrasts so that they evoke the same amount of suppression. Then the effective time constants (the rate at which the responses rise after lifting off from zero) should all be the same, and the oscillation amplitudes and frequencies should all be the same. On the other hand, there are many other combinations of target and mask contrasts that give the same mean firing rate but with different amounts of normalization (e.g., lower target contrast and lower mask contrast), and they should each evoke responses with different effective time constants and different oscillation amplitudes and frequencies.

- The effects shown in **Figs. 4d-f** (increasing responsivity of both low and high temporal-frequencies with increasing contrast, and shifting response phases in opposite directions for temporal frequencies above and below the preferred temporal frequency) may be evident for neurons with narrow temporal-frequency tuning, e.g., perhaps direction-selective neurons in layer 4b.

Acknowledgements

Funding: None

Special thanks to Mike Landy, Adam Kohn, Matteo Carandini, and Lyndon Duong for comments and discussion.

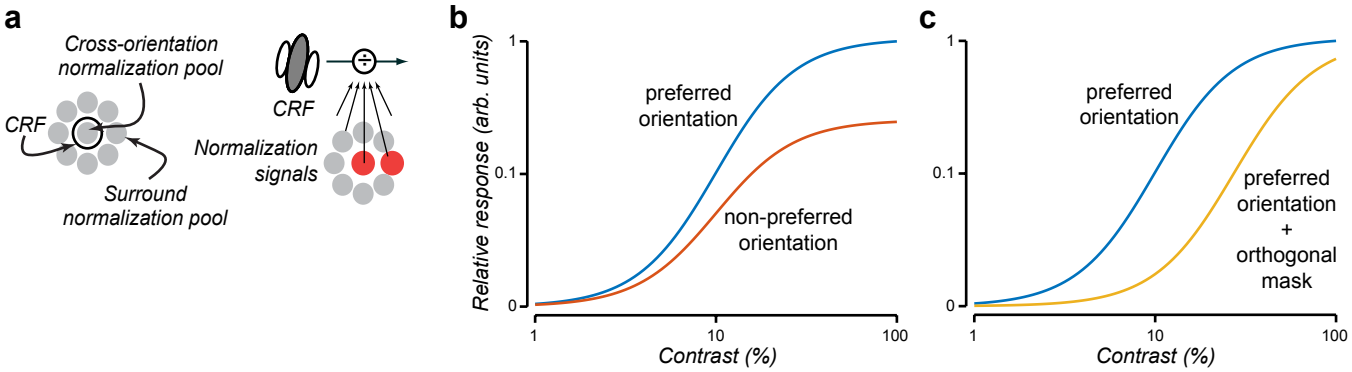

Figure 1. Normalization model. a. Conceptual diagram of normalization in which the neuron's response depends on a weighted sum of activity of a pool of neurons. **b.** Response saturation. Blue, responses to preferred stimulus orientation saturate at high contrasts. Orange, responses to non-preferred orientation are a scaled-down copy of the responses to preferred orientation, saturating at the same contrast. **c.** Cross-orientation suppression. Blue, preferred orientation. Yellow, superimposing an orthogonal stimulus (fixed contrast) suppresses responses to the preferred orientation. A similar result would be observed by adding a stimulus component that surrounds the preferred stimulus (surround suppression).

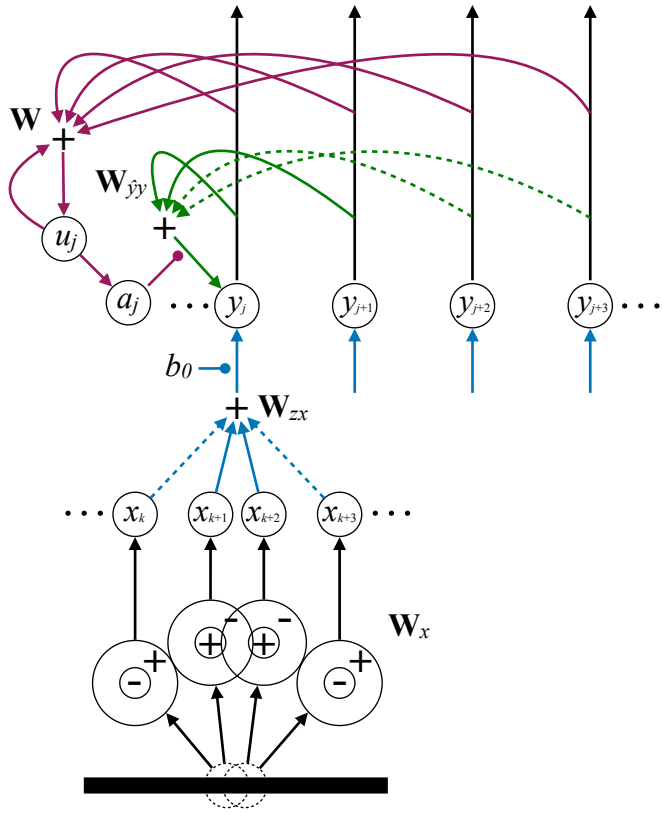

Figure 2. Recurrent circuit. Thick horizontal bar, input stimulus. Dotted circles, LGN receptive field locations. Different cell types: x_k, LGN inputs; y_j, simple cells; u_j and a_j, modulators. Synaptic weights: $\mathbf{W}_x$, center-surround weights determine LGN receptive fields; $\mathbf{W}_{zx}$, orientation-selective weights determine input drive to simple cells; $\mathbf{W}_{\hat{y}y}$, recurrent weights; $\mathbf{W}$, normalization weights. Solid lines, excitatory connections. Dashed lines, inhibitory connections. Circle heads, modulatory connections. Blue, input drive. Green, recurrent drive. Purple, modulatory drive.

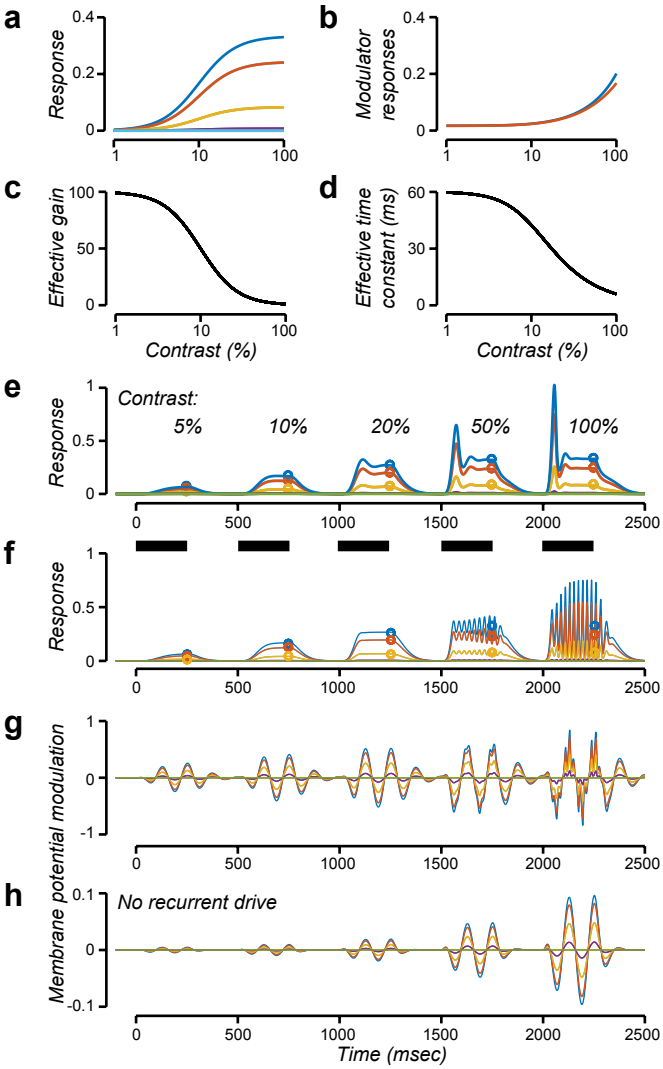

Figure 3. Recurrent amplification, effective time constant, onset transients, and oscillations. a. Response amplitudes of simulated simple- and complex-cells as a function of grating contrast. Different colors correspond to different orientation preferences. **b.** Response amplitudes of the modulator neurons: a (blue curve) and square root of u (orange curve). **c.** Effective gain (i.e., the ratio of y to z^2). **d.** Effective time constant. **e.** Response dynamics of simulated complex cells for a sequence of stimulus contrasts. Thick horizontal bars, each stimulus presentation was 250 ms. Stimulus contrasts: 5, 10, 20, 50, and 100%. Different colors correspond to different orientation preferences. Open circles, steady state response amplitudes (from panel **a**). Modulator time constant $\tau_u=10$ ms. **f.** Response dynamics of simulated complex cells for $\tau_u=1$ ms. **g.** Membrane potential responses (v) of simulated simple cells for $\tau_u=1$ ms. Different colors correspond to different orientation preferences, all with the same temporal phase. **h.** Membrane potential responses of simulated simple cells, but with recurrent amplification disabled (note smaller y-scale).

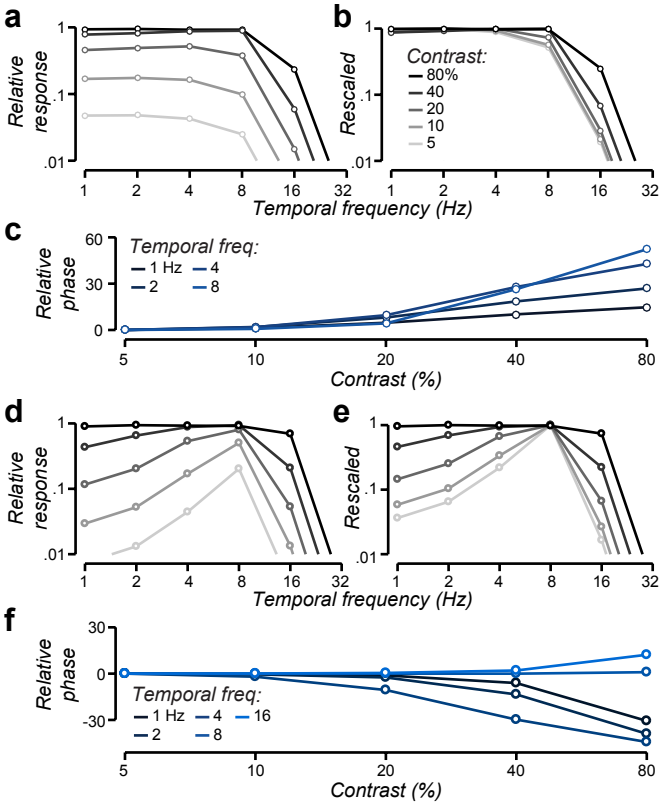

Figure 4. Temporal-frequency tuning and phase advance depend on contrast. a-c. Lowpass temporal-frequency tuning (ω=0 Hz). **a.** Response amplitudes for each of several stimulus temporal frequencies. Different shades of gray correspond to different stimulus contrasts: 5, 10, 20, 40, 80%. **b.** Rescaled responses. The different curves (from panel **a**) are each rescaled to have the same maximum so that the shapes of the curves can be readily compared. Responses to high contrasts (darker curves) are elevated compared to the responses to low contrasts (lighter curves). **c.** Phase advance. Response phase for each of several contrasts. Different colors corresponds to a different temporal frequencies: 1 2, 4, 8 Hz. **d-f.** Bandpass temporal-frequency tuning (ω=8 Hz).

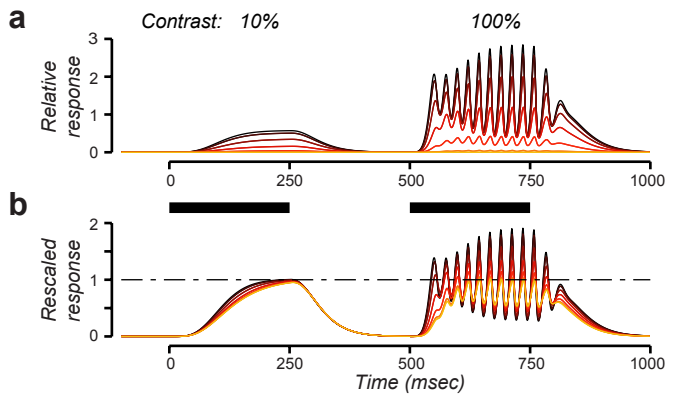

Figure 5. Response dynamics depend on stimulus location. a. Response dynamics of simulated complex cells for two contrasts (10% and 100%). Different colors correspond to different RF centers. Thick horizontal bars, stimulus presentations. **b.** Rescaled responses. The different curves (from panel **a**) are each rescaled by the corresponding fixed point, so that the shapes of the curves can be readily compared. The rate of response increase following stimulus onset is faster for stimuli placed in the center of a receptive field (darker colors) and slower on the flanks of the receptive field (lighter colors).

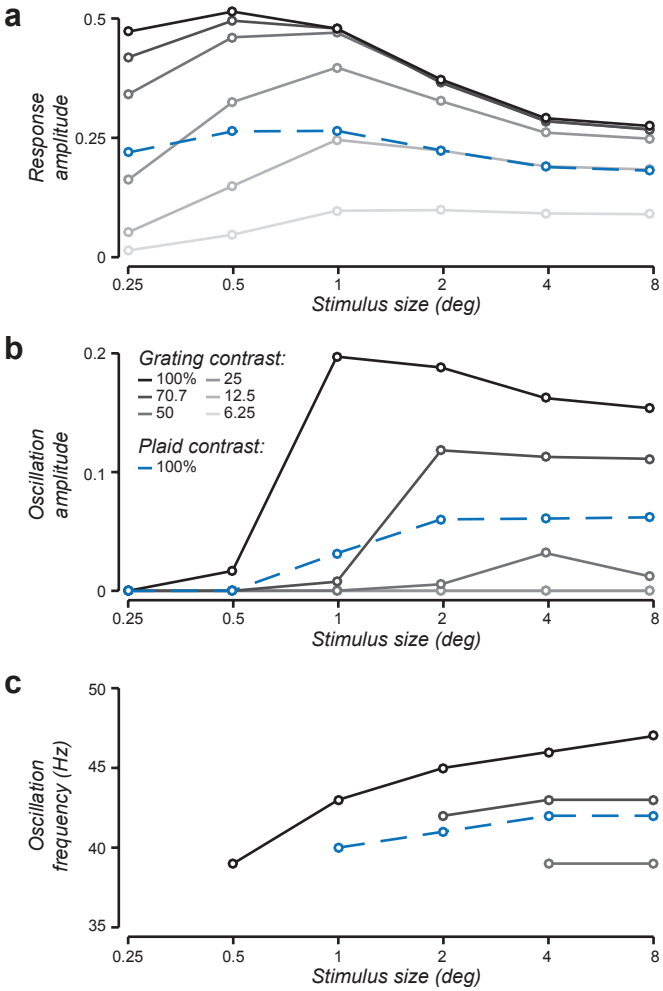

Figure 6. Oscillations depend on stimulus contrast and size. a. Surround suppression and cross-orientation suppression. Gray curves, response amplitudes to preferred-orientation gratings with each of several stimulus sizes. Different shades of gray correspond to different stimulus contrasts: 6.25, 12.5, 25, 50, and 100%. Dashed blue curve, 100% contrast plaid composed of a pair of orthogonal gratings (each 50% contrast). **b.** Oscillation amplitudes (computed by summing the Fourier amplitudes of the responses between 30-200 Hz, ignoring the first 250 ms of the responses after stimulus onset). Oscillations are evident only for the highest contrasts and increase with both stimulus contrast and stimulus size. **c.** Oscillation frequencies (shown only for those stimulus contrasts and sizes for which the oscillations are readily evident).

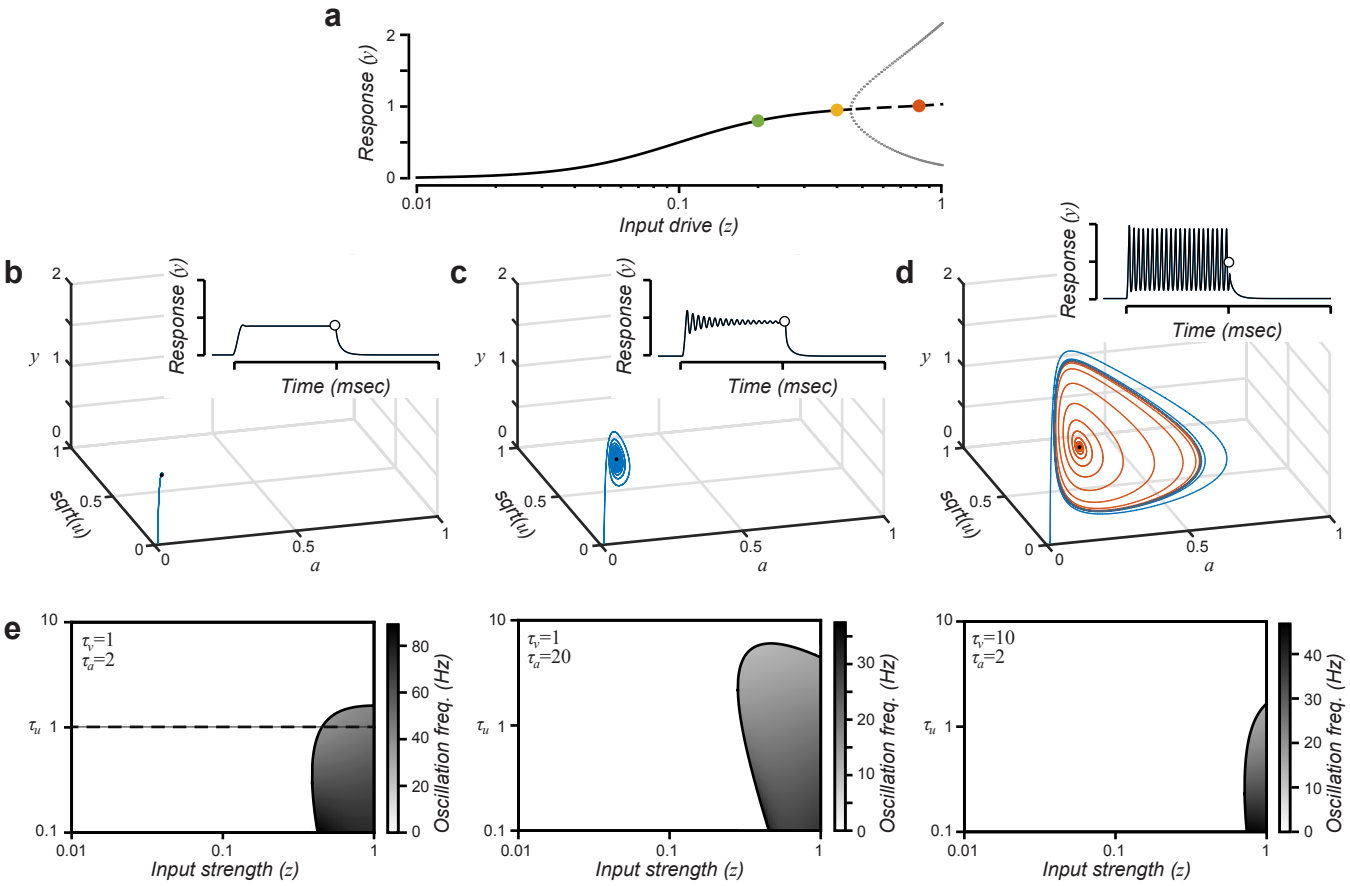

Figure 7. Phase space trajectories and bifurcation analysis. a. Bifurcation analysis as a function of input drive. Solid curve, stable fixed point (i.e., attractor). Dashed curve, unstable fixed point. Dotted gray curves, maximum and minimum of oscillations. Green, yellow, and orange dots correspond to phase space trajectories in panels **b**, **c**, and **d**, respectively. **b.** Phase space trajectory for a stable fixed point, corresponding to the green dot in panel **a** (z=0.2). Blue curve, time course of responses of the 3 simulated neurons for an initial condition in which all 3 have responses equal to zero. Black dot indicates the fixed point. Inset, response time course (open circle, fixed point). **c.** Phase space trajectory for a spiral attractor, corresponding to the yellow dot in panel **a** (z=0.4). **d.** Phase space trajectory for an unstable fixed point with stable limit cycle, corresponding to the orange dot in panel **a** (z=0.8). Blue curve, time course of responses of the 3 simulated neurons for an initial condition in which all 3 have responses equal to zero. Orange curve, time course of responses for an initial condition that is a slight (1%) perturbation from the fixed point. The blue curve spirals into the limit cycle and the orange curve spirals out from near the fixed point to the limit cycle. The responses traverse a curved manifold (shaped like a saddle or potato chip). **e.** Bifurcation analysis as a function of input drive (z) and time constant parameters (τ_v, τ_a and τ_u). Other model parameters: b_0=0.2, σ=0.1. Responses in the circumscribed regions exhibit stable oscillations (unstable fixed points with stable limit cycles). Grayscale indicates oscillation frequency. Dashed line corresponds to panel **a**.

References

1. D. J. Heeger, Normalization of cell responses in cat striate cortex. *Vis Neurosci* **9**, 181-197 (1992).
2. M. Carandini, D. J. Heeger, Normalization as a canonical neural computation. *Nat Rev Neurosci* **13**, 51-62 (2011).
3. D. G. Albrecht, W. S. Geisler, Motion sensitivity and the contrast-response function of simple cells in the visual cortex. *Visual Neuroscience* **7**, 531-546 (1991).
4. D. J. Heeger, "Nonlinear model of neural responses in cat visual cortex" in Computational models of visual processing, M. S. Landy, J. A. Movshon, Eds. (MIT Press, Cambridge, MA, 1991), pp. 119-133.
5. D. J. Heeger, Modeling simple-cell direction selectivity with normalized, half- squared, linear operators. *J Neurophysiol* **70**, 1885-1898 (1993).
6. M. Carandini, D. J. Heeger, Summation and division by neurons in primate visual cortex. *Science* **264**, 1333-1336 (1994).
7. E. P. Simoncelli, D. J. Heeger, A model of neuronal responses in visual area MT. *Vision research* **38**, 743-761 (1998).
8. O. Schwartz, E. P. Simoncelli, Natural signal statistics and sensory gain control. *Nat Neurosci* **4**, 819-825 (2001).
9. O. Schwartz, E. P. Simoncelli (2001) Natural sound statistics and divisive normalization in the auditory system. in *Advances in neural information processing systems*, pp 166-172.
10. M. J. Wainwright, O. Schwartz, E. P. Simoncelli, "Natural Image Statistics and Divisive Normalization" in Probabilistic Models of the Brain: Perception and Neural Function, R. P. N. Rao, B. A. Olshausen, M. S. Lewicki, Eds. (MIT Press, 2002), pp. 203-.
11. D. Zoccolan, D. D. Cox, J. J. DiCarlo, Multiple object response normalization in monkey inferotemporal cortex. *J Neurosci* **25**, 8150-8164 (2005).
12. N. C. Rust, V. Mante, E. P. Simoncelli, J. A. Movshon, How MT cells analyze the motion of visual patterns. *Nat Neurosci* **9**, 1421-1431 (2006).
13. T. Sugihara, M. D. Diltz, B. B. Averbeck, L. M. Romanski, Integration of auditory and visual communication information in the primate ventrolateral prefrontal cortex. *J Neurosci* **26**, 11138-11147 (2006).
14. M. Avillac, S. Ben Hamed, J. R. Duhamel, Multisensory integration in the ventral intraparietal area of the macaque monkey. *J Neurosci* **27**, 1922-1932 (2007).
15. G. M. Boynton, A framework for describing the effects of attention on visual responses. *Vision Res* **49**, 1129-1143 (2009).
16. L. Busse, A. R. Wade, M. Carandini, Representation of concurrent stimuli by population activity in visual cortex. *Neuron* **64**, 931-942 (2009).
17. J. Lee, J. H. Maunsell, A normalization model of attentional modulation of single unit responses. *PLoS ONE* **4**, e4651 (2009).
18. F. Moradi, D. J. Heeger, Inter-ocular contrast normalization in human visual cortes. *Journal of vision* **9(3)**, 1-22 (2009).
19. J. H. Reynolds, D. J. Heeger, The normalization model of attention. *Neuron* **61**, 168-185 (2009).
20. K. A. Sundberg, J. F. Mitchell, J. H. Reynolds, Spatial attention modulates center-surround interactions in macaque visual area v4. *Neuron* **61**, 952-963 (2009).
21. K. Herrmann, L. Montaser-Kouhsari, M. Carrasco, D. J. Heeger, When size matters: attention affects performance by contrast or response gain. *Nat Neurosci* **13**, 1554-1559 (2010).

22. P. S. Khayat, R. Niebergall, J. C. Martinez-Trujillo, Attention differentially modulates similar neuronal responses evoked by varying contrast and direction stimuli in area MT. *J Neurosci* **30**, 2188-2197 (2010).

23. J. Lee, J. H. Maunsell, Attentional modulation of MT neurons with single or multiple stimuli in their receptive fields. *J Neurosci* **30**, 3058-3066 (2010).

24. S. R. Olsen, V. Bhandawat, R. I. Wilson, Divisive normalization in olfactory population codes. *Neuron* **66**, 287-299 (2010).

25. G. J. Brouwer, D. J. Heeger, Cross-orientation suppression in human visual cortex. *Journal of neurophysiology* **106**, 2108-2119 (2011).

26. K. Louie, L. E. Grattan, P. W. Glimcher, Reward value-based gain control: divisive normalization in parietal cortex. *The Journal of neuroscience : the official journal of the Society for Neuroscience* **31**, 10627-10639 (2011).

27. T. Ohshiro, D. E. Angelaki, G. C. Deangelis, A normalization model of multisensory integration. *Nature neuroscience* **14**, 775-782 (2011).

28. N. C. Rabinowitz, B. D. Willmore, J. W. Schnupp, A. J. King, Contrast gain control in auditory cortex. *Neuron* **70**, 1178-1191 (2011).

29. T. Lochmann, U. A. Ernst, S. Deneve, Perceptual inference predicts contextual modulations of sensory responses. *J Neurosci* **32**, 4179-4195 (2012).

30. K. Louie, M. W. Khaw, P. W. Glimcher, Normalization is a general neural mechanism for context-dependent decision making. *Proc Natl Acad Sci U S A* **110**, 6139-6144 (2013).

31. S. Ray, A. M. Ni, J. H. Maunsell, Strength of gamma rhythm depends on normalization. *PLoS Biol* **11**, e1001477 (2013).

32. O. Schwartz, R. Coen-Cagli, Visual attention and flexible normalization pools. *J Vis* **13** (2013).

33. M. M. Diehl, L. M. Romanski, Responses of prefrontal multisensory neurons to mismatching faces and vocalizations. *J Neurosci* **34**, 11233-11243 (2014).

34. Y. Hara, F. Pestilli, J. L. Gardner, Differing effects of attention in single-units and populations are well predicted by heterogeneous tuning and the normalization model of attention. *Frontiers in computational neuroscience* **8**, 12 (2014).

35. K. Louie, T. LoFaro, R. Webb, P. W. Glimcher, Dynamic divisive normalization predicts time-varying value coding in decision-related circuits. *J Neurosci* **34**, 16046-16057 (2014).

36. T. K. Sato, M. Hausser, M. Carandini, Distal connectivity causes summation and division across mouse visual cortex. *Nat Neurosci* **17**, 30-32 (2014).

37. S. G. Solomon, A. Kohn, Moving sensory adaptation beyond suppressive effects in single neurons. *Curr Biol* **24**, R1012-1022 (2014).

38. G. J. Brouwer, V. Arnedo, S. Offen, D. J. Heeger, A. C. Grant, Normalization in human somatosensory cortex. *J Neurophysiol* **114**, 2588-2599 (2015).

39. J. J. Nassi, M. C. Avery, A. H. Cetin, A. W. Roe, J. H. Reynolds, Optogenetic Activation of Normalization in Alert Macaque Visual Cortex. *Neuron* **86**, 1504-1517 (2015).

40. M. Snow, R. Coen-Cagli, O. Schwartz, Specificity and timescales of cortical adaptation as inferences about natural movie statistics. *J Vis* **16** (2016).

41. B. E. Verhoef, J. H. Maunsell, Attention operates uniformly throughout the classical receptive field and the surround. *Elife* **5** (2016).

42. Z. M. Westrick, D. J. Heeger, M. S. Landy, Pattern Adaptation and Normalization Reweighting. *J Neurosci* **36**, 9805-9816 (2016).

43. M. W. Khaw, P. W. Glimcher, K. Louie, Normalized value coding explains dynamic adaptation in the human valuation process. *Proc Natl Acad Sci U S A* **114**, 12696-12701 (2017).

44. A. M. Ni, J. H. R. Maunsell, Spatially tuned normalization explains attention modulation variance within neurons. *J Neurophysiol* **118**, 1903-1913 (2017).

45. T. Ohshiro, D. E. Angelaki, G. C. DeAngelis, A Neural Signature of Divisive Normalization at the Level of Multisensory Integration in Primate Cortex. *Neuron* **95**, 399-411 e398 (2017).

46. B. E. Verhoef, J. H. R. Maunsell, Attention-related changes in correlated neuronal activity arise from normalization mechanisms. *Nat Neurosci* **20**, 969-977 (2017).

47. A. Aschner, S. G. Solomon, M. S. Landy, D. J. Heeger, A. Kohn, Temporal Contingencies Determine Whether Adaptation Strengthens or Weakens Normalization. *J Neurosci* **38**, 10129-10142 (2018).

48. M. C. Morrone, D. C. Burr, L. Maffei, Functional implications of cross-orientation inhibition of cortical visual cells. *Proceedings of the Royal Society of London, B* **216**, 335-354 (1982).

49. M. C. Morrone, D. C. Burr, Evidence for the existence and development of visual inhibition in humans. *Nature* **321**, 235-237 (1986).

50. M. Carandini, D. J. Heeger, J. A. Movshon, Linearity and normalization in simple cells of the macaque primary visual cortex. *J Neurosci* **17**, 8621-8644 (1997).

51. D. J. Tolhurst, D. J. Heeger, Comparison of contrast-normalization and threshold models of the responses of simple cells in cat striate cortex. *Vis Neurosci* **14**, 293-309 (1997).

52. D. J. Tolhurst, D. J. Heeger, Contrast normalization and a linear model for the directional selectivity of simple cells in cat striate cortex. *Vis Neurosci* **14**, 19-25 (1997).

53. M. P. Sceniak, D. L. Ringach, M. J. Hawken, R. Shapley, Contrast's effect on spatial summation by macaque V1 neurons. *Nat Neurosci* **2**, 733-739 (1999).

54. M. P. Sceniak, M. J. Hawken, R. Shapley, Visual spatial characterization of macaque V1 neurons. *J Neurophysiol* **85**, 1873-1887. (2001).

55. J. R. Cavanaugh, W. Bair, J. A. Movshon, Nature and interaction of signals from the receptive field center and surround in macaque V1 neurons. *J Neurophysiol* **88**, 2530-2546. (2002).

56. J. R. Cavanaugh, W. Bair, J. A. Movshon, Selectivity and spatial distribution of signals from the receptive field surround in macaque V1 neurons. *J Neurophysiol* **88**, 2547-2556. (2002).

57. B. Zenger-Landolt, D. J. Heeger, Response suppression in V1 agrees with psychophysics of surround masking. *J Neurosci* **23**, 6884-6893 (2003).

58. M. A. Smith, W. Bair, J. A. Movshon, Dynamics of suppression in macaque primary visual cortex. *J Neurosci* **26**, 4826-4834 (2006).

59. J. M. Foley, Human luminance pattern-vision mechanisms: masking experiments require a new model. *J Opt Soc Am A* **11**, 1710-1719. (1994).

60. J. Xing, D. J. Heeger, Center-surround interactions in foveal and peripheral vision. *Vision Res* **40**, 3065-3072 (2000).

61. J. Xing, D. J. Heeger, Measurement and modeling of center-surround suppression and enhancement. *Vision Res* **41**, 571-583. (2001).

62. Y. Petrov, M. Carandini, S. McKee, Two distinct mechanisms of suppression in human vision. *J Neurosci* **25**, 8704-8707 (2005).

63. H. Yiltiz, D. J. Heeger, M. S. Landy, Contingent adaptation in masking and surround suppression. *Vision Res* **166**, 72-80 (2020).

64. A. B. Bonds, Role of inhibition in the specification of orientation selectivity of cells in the cat striate cortex. *Vis Neurosci* **2**, 41-55 (1989).

65. G. C. DeAngelis, J. G. Robson, I. Ohzawa, R. D. Freeman, Organization of suppression in receptive fields of neurons in cat visual cortex. *J Neurophysiol* **68**, 144-163 (1992).

66. G. C. DeAngelis, R. D. Freeman, I. Ohzawa, Length and width tuning of neurons in the cat's primary visual cortex. *J Neurophysiol* **71**, 347-374 (1994).

67. W. Bair, J. R. Cavanaugh, J. A. Movshon, Time course and time-distance relationships for surround suppression in macaque V1 neurons. *J Neurosci* **23**, 7690-7701 (2003).

68. Y. F. Sit, Y. Chen, W. S. Geisler, R. Miikkulainen, E. Seidemann, Complex dynamics of V1 population responses explained by a simple gain-control model. *Neuron* **64**, 943-956 (2009).

69. R. A. Holub, M. Morton-Gibson, Response of Visual Cortical Neurons of the cat to moving sinusoidal gratings: response-contrast functions and spatiotemporal interactions. *J Neurophysiol* **46**, 1244-1259 (1981).

70. A. F. Dean, D. J. Tolhurst, Factors influencing the temporal phase of response to bar and grating stimuli for simple cells in the cat striate cortex. *Experimental Brain Research* **62**, 143-151 (1986).

71. D. G. Albrecht, Visual cortex neurons in monkey and cat: Effect of contrast on the spatial and temporal phase transfer functions. *Visual Neuroscience* **12**, 1191-1210 (1995).

72. M. A. Gieselmann, A. Thiele, Comparison of spatial integration and surround suppression characteristics in spiking activity and the local field potential in macaque V1. *Eur J Neurosci* **28**, 447-459 (2008).

73. C. Kayser, R. F. Salazar, P. Konig, Responses to natural scenes in cat V1. *J Neurophysiol* **90**, 1910-1920 (2003).

74. J. A. Henrie, R. Shapley, LFP power spectra in V1 cortex: the graded effect of stimulus contrast. *J Neurophysiol* **94**, 479-490 (2005).

75. Z. Zhou, M. R. Bernard, A. B. Bonds, Deconstruction of spatial integrity in visual stimulus detected by modulation of synchronized activity in cat visual cortex. *J Neurosci* **28**, 3759-3768 (2008).

76. B. Lima, W. Singer, N. H. Chen, S. Neuenschwander, Synchronization dynamics in response to plaid stimuli in monkey V1. *Cereb Cortex* **20**, 1556-1573 (2010).

77. S. Ray, J. H. Maunsell, Differences in gamma frequencies across visual cortex restrict their possible use in computation. *Neuron* **67**, 885-896 (2010).

78. M. J. Bartolo *et al.*, Stimulus-induced dissociation of neuronal firing rates and local field potential gamma power and its relationship to the resonance blood oxygen level-dependent signal in macaque primary visual cortex. *Eur J Neurosci* **34**, 1857-1870 (2011).

79. X. Jia, A. Kohn, Gamma rhythms in the brain. *PLoS Biol* **9**, e1001045 (2011).

80. X. Jia, M. A. Smith, A. Kohn, Stimulus selectivity and spatial coherence of gamma components of the local field potential. *J Neurosci* **31**, 9390-9403 (2011).

81. S. Ray, J. H. Maunsell, Different origins of gamma rhythm and high-gamma activity in macaque visual cortex. *PLoS Biol* **9**, e1000610 (2011).

82. X. Jia, D. Xing, A. Kohn, No consistent relationship between gamma power and peak frequency in macaque primary visual cortex. *J Neurosci* **33**, 17-25 (2013).

83. D. Hermes, K. J. Miller, B. A. Wandell, J. Winawer, Stimulus Dependence of Gamma Oscillations in Human Visual Cortex. *Cereb Cortex* **25**, 2951-2959 (2015).

84. M. W. Self *et al.*, The Effects of Context and Attention on Spiking Activity in Human Early Visual Cortex. *PLoS Biol* **14**, e1002420 (2016).

85. E. Bartoli *et al.*, Functionally Distinct Gamma Range Activity Revealed by Stimulus Tuning in Human Visual Cortex. *Curr Biol* **29**, 3345-3358 e3347 (2019).

86. N. M. Brunet, P. Fries, Human visual cortical gamma reflects natural image structure. *NeuroImage* **200**, 635-643 (2019).

87. H. Adesnik, M. Scanziani, Lateral competition for cortical space by layer-specific horizontal circuits. *Nature* **464**, 1155-1160 (2010).

88. T. K. Sato, B. Haider, M. Hausser, M. Carandini, An excitatory basis for divisive normalization in visual cortex. *Nat Neurosci* **19**, 568-570 (2016).

89. H. Adesnik, Synaptic Mechanisms of Feature Coding in the Visual Cortex of Awake Mice. *Neuron* **95**, 1147-1159 e1144 (2017).

90. K. A. Bolding, K. M. Franks, Recurrent cortical circuits implement concentration-invariant odor coding. *Science* **361** (2018).

91. R. J. Douglas, C. Koch, M. Mahowald, K. A. Martin, H. H. Suarez, Recurrent excitation in neocortical circuits. *Science* **269**, 981-985. (1995).

92. E. M. Callaway, Local circuits in primary visual cortex of the macaque monkey. *Annu Rev Neurosci* **21**, 47-74 (1998).

93. Y. Yoshimura, J. L. Dantzker, E. M. Callaway, Excitatory cortical neurons form fine-scale functional networks. *Nature* **433**, 868-873 (2005).

94. R. J. Douglas, K. A. Martin, Recurrent neuronal circuits in the neocortex. *Curr Biol* **17**, R496-500 (2007).

95. C. Kapfer, L. L. Glickfeld, B. V. Atallah, M. Scanziani, Supralinear increase of recurrent inhibition during sparse activity in the somatosensory cortex. *Nat Neurosci* **10**, 743-753 (2007).

96. S. Peron *et al.*, Recurrent interactions in local cortical circuits. *Nature* **579**, 256-259 (2020).

97. M. Carandini, D. J. Heeger, W. Senn, A synaptic explanation of suppression in visual cortex. *J Neurosci* **22**, 10053-10065. (2002).

98. H. Ozeki, I. M. Finn, E. S. Schaffer, K. D. Miller, D. Ferster, Inhibitory stabilization of the cortical network underlies visual surround suppression. *Neuron* **62**, 578-592 (2009).

99. T. Brosch, H. Neumann, Computing with a canonical neural circuits model with pool normalization and modulating feedback. *Neural Comput* **26**, 2735-2789 (2014).

100. D. B. Rubin, S. D. Van Hooser, K. D. Miller, The stabilized supralinear network: a unifying circuit motif underlying multi-input integration in sensory cortex. *Neuron* **85**, 402-417 (2015).

101. E. Koch, J. Jin, J. M. Alonso, Q. Zaidi, Functional implications of orientation maps in primary visual cortex. *Nat Commun* **7**, 13529 (2016).

102. D. J. Heeger, K. O. Zemlianova (2020) Supplemental Material for “Dynamic Normalization”. (NYU Faculty Digial Archive, https://archive.nyu.edu/handle/2451/61045).

103. D. J. Heeger, W. E. Mackey, ORGaNICs: A Theory of Working Memory in Brains and Machines. *arXiv preprint arXiv:1803.06288* (2018).

104. D. J. Heeger, W. E. Mackey, ORGaNICs: A Canonical Neural Circuit Computation. *bioRxiv*, 506337 (2018).

105. D. J. Heeger, W. E. Mackey, Oscillatory recurrent gated neural integrator circuits (ORGaNICs), a unifying theoretical framework for neural dynamics. *Proc Natl Acad Sci U S A* **116**, 22783-22794 (2019).

106. D. J. Heeger, Half-squaring in responses of cat striate cells. *Vis Neurosci* **9**, 427-443 (1992).

107. E. H. Adelson, J. R. Bergen, Spatiotemporal energy models for the perception of motion. *Journal of the Optical Society of America A* **2**, 284-299 (1985).

108. J. C. Horton, W. F. Hoyt, The representation of the visual field in human striate cortex. *Archives of Ophthalmology* **109**, 816-824 (1991).

109. S. O. Dumoulin, B. A. Wandell, Population receptive field estimates in human visual cortex. *NeuroImage* **39**, 647-660 (2008).

110. J. Winawer, H. Horiguchi, R. A. Sayres, K. Amano, B. A. Wandell, Mapping hV4 and ventral occipital cortex: the venous eclipse. *J Vis* **10**, 1 (2010).

111. J. Freeman, E. P. Simoncelli, Metamers of the ventral stream. *Nat Neurosci* **14**, 1195-1201 (2011).

112. K. N. Kay, J. Winawer, A. Mezer, B. A. Wandell, Compressive spatial summation in human visual cortex. *J Neurophysiol* **110**, 481-494 (2013).

113. D. J. T. N. S. Walker, I. D. Thompson, A. F. Dean, Nonlinearities of temporal summation in neurones in area 17 of the cat. *Experimental Brain Research* **38**, 431-435 (1980).

114. A. F. Dean, D. J. Tolhurst, On the distinctness of simple and complex cells in the visual cortex of the cat. *J Physiol* **344**, 305-325 (1983).

115. D. G. Albrecht, W. S. Geisler, R. A. Frazor, A. M. Crane, Visual cortex neurons of monkeys and cats: temporal dynamics of the contrast response function. *J Neurophysiol* **88**, 888-913 (2002).

116. W. Bair, J. R. Cavanaugh, M. A. Smith, J. A. Movshon, The timing of response onset and offset in macaque visual neurons. *J Neurosci* **22**, 3189-3205. (2002).

117. S. P. Burns, D. Xing, R. M. Shapley, Comparisons of the dynamics of local field potential and multiunit activity signals in macaque visual cortex. *J Neurosci* **30**, 13739-13749 (2010).

118. J. Zhou, N. C. Benson, K. N. Kay, J. Winawer, Compressive Temporal Summation in Human Visual Cortex. *J Neurosci* **38**, 691-709 (2018).

119. J. R. Muller, A. B. Metha, J. Krauskopf, P. Lennie, Rapid adaptation in visual cortex to the structure of images. *Science* **285**, 1405-1408. (1999).

120. J. R. Muller, A. B. Metha, J. Krauskopf, P. Lennie, Information conveyed by onset transients in responses of striate cortical neurons. *J Neurosci* **21**, 6978-6990. (2001).

121. D. L. Ringach, M. J. Hawken, R. Shapley, Dynamics of orientation tuning in macaque primary visual cortex. *Nature* **387**, 281-284 (1997).

122. D. Ferster, S. Chung, H. S. Wheat, Orientation selectivity of synaptic input from lateral geniculate nucleus to simple cells of cat visual cortex. *Nature* **380**, 249-252 (1996).

123. S. Chung, D. Ferster, Strength and orientation tuning of the thalamic input to simple cells revealed by electrically evoked cortical suppression. *Neuron* **20**, 1177-1189 (1998).

124. K. Reinhold, A. D. Lien, M. Scanziani, Distinct recurrent versus afferent dynamics in cortical visual processing. *Nat Neurosci* **18**, 1789-1797 (2015).

125. A. D. Lien, M. Scanziani, Cortical direction selectivity emerges at convergence of thalamic synapses. *Nature* **558**, 80-86 (2018).

126. S. Hochreiter, J. Schmidhuber, Long short-term memory. *Neural Comput* **9**, 1735-1780 (1997).

127. R. Eckhorn *et al.*, Coherent oscillations: a mechanism of feature linking in the visual cortex? Multiple electrode and correlation analyses in the cat. *Biol Cybern* **60**, 121-130 (1988).

128. C. M. Gray, P. Konig, A. K. Engel, W. Singer, Oscillatory responses in cat visual cortex exhibit inter-columnar synchronization which reflects global stimulus properties. *Nature* **338**, 334-337 (1989).

129. W. Singer, Neuronal synchrony: a versatile code for the definition of relations? *Neuron* **24**, 49-65, 111-125. (1999).

130. A. K. Engel, P. Fries, W. Singer, Dynamic predictions: oscillations and synchrony in top-down processing. *Nat Rev Neurosci* **2**, 704-716 (2001).

131. H. Tiitinen *et al.*, Selective attention enhances the auditory 40-Hz transient response in humans. *Nature* **364**, 59-60 (1993).

132. P. Fries, J. H. Reynolds, A. E. Rorie, R. Desimone, Modulation of oscillatory neuronal synchronization by selective visual attention. *Science* **291**, 1560-1563. (2001).

133. E. Salinas, T. J. Sejnowski, Correlated neuronal activity and the flow of neural information. *Nat Rev Neurosci* **2**, 539-550 (2001).

134. G. Deco, A. Thiele, Attention: oscillations and neuropharmacology. *Eur J Neurosci* **30**, 347-354 (2009).

135. M. Abeles, Role of the cortical neuron: integrator or coincidence detector? *Isr J Med Sci* **18**, 83-92 (1982).

136. P. Konig, A. K. Engel, W. Singer, Integrator or coincidence detector? The role of the cortical neuron revisited. *Trends Neurosci* **19**, 130-137 (1996).

137. F. Varela, J. P. Lachaux, E. Rodriguez, J. Martinerie, The brainweb: phase synchronization and large-scale integration. *Nat Rev Neurosci* **2**, 229-239 (2001).

138. P. Fries, A mechanism for cognitive dynamics: neuronal communication through neuronal coherence. *Trends Cogn Sci* **9**, 474-480 (2005).

139. C. Borgers, N. J. Kopell, Gamma oscillations and stimulus selection. *Neural Comput* **20**, 383-414 (2008).

140. P. Fries, Neuronal gamma-band synchronization as a fundamental process in cortical computation. *Annu Rev Neurosci* **32**, 209-224 (2009).

141. G. G. Gregoriou, S. J. Gotts, H. Zhou, R. Desimone, High-frequency, long-range coupling between prefrontal and visual cortex during attention. *Science* **324**, 1207-1210 (2009).

142. T. Akam, D. M. Kullmann, Oscillations and filtering networks support flexible routing of information. *Neuron* **67**, 308-320 (2010).

143. S. P. Burns, D. Xing, M. J. Shelley, R. M. Shapley, Searching for autocoherence in the cortical network with a time-frequency analysis of the local field potential. *J Neurosci* **30**, 4033-4047 (2010).

144. M. Chalk *et al.*, Attention reduces stimulus-driven gamma frequency oscillations and spike field coherence in V1. *Neuron* **66**, 114-125 (2010).

145. S. P. Burns, D. Xing, R. M. Shapley, Is gamma-band activity in the local field potential of V1 cortex a "clock" or filtered noise? *J Neurosci* **31**, 9658-9664 (2011).

146. D. Xing *et al.*, Stochastic generation of gamma-band activity in primary visual cortex of awake and anesthetized monkeys. *J Neurosci* **32**, 13873-13880a (2012).

147. D. Hermes, K. J. Miller, B. A. Wandell, J. Winawer, Gamma oscillations in visual cortex: the stimulus matters. *Trends Cogn Sci* **19**, 57-58 (2015).

148. V. Shirhatti, S. Ray, Long-wavelength (reddish) hues induce unusually large gamma oscillations in the primate primary visual cortex. *Proc Natl Acad Sci U S A* **115**, 4489-4494 (2018).

149. L. M. Hurvich, D. Jameson, An opponent-process theory of color vision. *Psychol Rev* **64, Part 1**, 384-404 (1957).

150. A. M. Derrington, J. Krauskopf, P. Lennie, Chromatic mechanisms in lateral geniculate nucleus of macaque. *J Physiol* **357**, 241-265 (1984).

151. P. K. Kaiser, R. M. Boynton, Human color vision. (1996).

152. W. J. Freeman, Relations between unit activity and evoked potentials in prepyriform cortex of cats. *J Neurophysiol* **31**, 337-348 (1968).

153. J. M. Horowitz, Evoked activity of single units and neural populations in the hippocampus of the cat. *Electroencephalogr Clin Neurophysiol* **32**, 227-240 (1972).

154. H. R. Wilson, J. D. Cowan, Excitatory and inhibitory interactions in localized populations of model neurons. *Biophys J* **12**, 1-24 (1972).

155. L. S. Leung, Nonlinear feedback model of neuronal populations in hippocampal CAI region. *J Neurophysiol* **47**, 845-868 (1982).

156. M. A. Whittington, R. D. Traub, J. G. Jefferys, Synchronized oscillations in interneuron networks driven by metabotropic glutamate receptor activation. *Nature* **373**, 612-615 (1995).

157. P. Bush, T. Sejnowski, Inhibition synchronizes sparsely connected cortical neurons within and between columns in realistic network models. *J Comput Neurosci* **3**, 91-110 (1996).

158. R. D. Traub, M. A. Whittington, I. M. Stanford, J. G. Jefferys, A mechanism for generation of long-range synchronous fast oscillations in the cortex. *Nature* **383**, 621-624 (1996).

159. R. D. Traub, J. G. Jefferys, M. A. Whittington, Simulation of gamma rhythms in networks of interneurons and pyramidal cells. *J Comput Neurosci* **4**, 141-150 (1997).

160. M. A. Whittington, R. D. Traub, N. Kopell, B. Ermentrout, E. H. Buhl, Inhibition-based rhythms: experimental and mathematical observations on network dynamics. *Int J Psychophysiol* **38**, 315-336 (2000).

161. P. Tiesinga, T. J. Sejnowski, Cortical enlightenment: are attentional gamma oscillations driven by ING or PING? *Neuron* **63**, 727-732 (2009).

162. K. Kang, M. Shelley, J. A. Henrie, R. Shapley, LFP spectral peaks in V1 cortex: network resonance and cortico-cortical feedback. *J Comput Neurosci* **29**, 495-507 (2010).

163. X. J. Wang, Neurophysiological and computational principles of cortical rhythms in cognition. *Physiol Rev* **90**, 1195-1268 (2010).

164. D. J. Field, A. Hayes, R. F. Hess, Contour integration by the human visual system: evidence for a local "association field". *Vision Res* **33**, 173-193 (1993).

165. Z. Li, A neural model of contour integration in the primary visual cortex. *Neural Comput* **10**, 903-940 (1998).

166. W. S. Geisler, J. S. Perry, B. J. Super, D. P. Gallogly, Edge co-occurrence in natural images predicts contour grouping performance. *Vision Res* **41**, 711-724 (2001).

167. R. F. Hess, W. H. Beaudot, K. T. Mullen, Dynamics of contour integration. *Vision Res* **41**, 1023-1037 (2001).

168. R. F. Hess, A. Hayes, D. J. Field, Contour integration and cortical processing. *Journal of physiology, Paris* **97**, 105-119 (2003).

169. U. A. Ernst *et al.*, Optimality of human contour integration. *PLoS Comput Biol* **8**, e1002520 (2012).

170. O. Bernander, R. J. Douglas, K. A. Martin, C. Koch, Synaptic background activity influences spatiotemporal integration in single pyramidal cells. *Proc Natl Acad Sci U S A* **88**, 11569-11573 (1991).

171. P. H. Tiesinga, J. M. Fellous, E. Salinas, J. V. Jose, T. J. Sejnowski, Inhibitory synchrony as a mechanism for attentional gain modulation. *Journal of physiology, Paris* **98**, 296-314 (2004).

172. K. Taylor, S. Mandon, W. A. Freiwald, A. K. Kreiter, Coherent oscillatory activity in monkey area v4 predicts successful allocation of attention. *Cereb Cortex* **15**, 1424-1437 (2005).

173. C. Borgers, S. Epstein, N. J. Kopell, Gamma oscillations mediate stimulus competition and attentional selection in a cortical network model. *Proc Natl Acad Sci U S A* **105**, 18023-18028 (2008).

174. P. Fries, T. Womelsdorf, R. Oostenveld, R. Desimone, The effects of visual stimulation and selective visual attention on rhythmic neuronal synchronization in macaque area V4. *J Neurosci* **28**, 4823-4835 (2008).

175. M. Vinck, T. Womelsdorf, E. A. Buffalo, R. Desimone, P. Fries, Attentional modulation of cell-class-specific gamma-band synchronization in awake monkey area v4. *Neuron* **80**, 1077-1089 (2013).

176. T. J. Gawne, T. W. Kjaer, B. J. Richmond, Latency: another potential code for feature binding in striate cortex. *J Neurophysiol* **76**, 1356-1360 (1996).

177. J. S. Anderson, I. Lampl, D. C. Gillespie, D. Ferster, The contribution of noise to contrast invariance of orientation tuning in cat visual cortex. *Science* **290**, 1968-1972 (2000).

178. M. Carandini, D. Ferster, Membrane potential and firing rate in cat primary visual cortex. *J Neurosci* **20**, 470-484 (2000).

179. K. D. Miller, T. W. Troyer, Neural noise can explain expansive, power-law nonlinearities in neural response functions. *J Neurophysiol* **87**, 653-659 (2002).

180. B. V. Atallah, W. Bruns, M. Carandini, M. Scanziani, Parvalbumin-expressing interneurons linearly transform cortical responses to visual stimuli. *Neuron* **73**, 159-170 (2012).

181. H. Adesnik, W. Bruns, H. Taniguchi, Z. J. Huang, M. Scanziani, A neural circuit for spatial summation in visual cortex. *Nature* **490**, 226-231 (2012).

182. A. Angelucci, J. B. Levitt, J. S. Lund, Anatomical origins of the classical receptive field and modulatory surround field of single neurons in macaque visual cortical area V1. *Prog Brain Res* **136**, 373-388 (2002).

183. A. Angelucci *et al.*, Circuits for local and global signal integration in primary visual cortex. *J Neurosci* **22**, 8633-8646. (2002).

184. J. J. Nassi, S. G. Lomber, R. T. Born, Corticocortical feedback contributes to surround suppression in V1 of the alert primate. *J Neurosci* **33**, 8504-8517 (2013).

185. J. J. Nassi, C. Gomez-Laberge, G. Kreiman, R. T. Born, Corticocortical feedback increases the spatial extent of normalization. *Front Syst Neurosci* **8**, 105 (2014).

186. N. D. Schiff *et al.*, Behavioural improvements with thalamic stimulation after severe traumatic brain injury. *Nature* **448**, 600-603 (2007).

187. B. B. Theyel, D. A. Llano, S. M. Sherman, The corticothalamocortical circuit drives higher-order cortex in the mouse. *Nat Neurosci* **13**, 84-88 (2010).

188. Y. B. Saalmann, M. A. Pinsk, L. Wang, X. Li, S. Kastner, The pulvinar regulates information transmission between cortical areas based on attention demands. *Science* **337**, 753-756 (2012).

189. Z. V. Guo *et al.*, Maintenance of persistent activity in a frontal thalamocortical loop. *Nature* **545**, 181-186 (2017).

190. L. I. Schmitt *et al.*, Thalamic amplification of cortical connectivity sustains attentional control. *Nature* **545**, 219-223 (2017).

191. R. V. Rikhye, A. Gilra, M. M. Halassa, Thalamic regulation of switching between cortical representations enables cognitive flexibility. *Nat Neurosci* **21**, 1753-1763 (2018).

192. R. V. Rikhye, R. D. Wimmer, M. M. Halassa, Toward an Integrative Theory of Thalamic Function. *Annual review of neuroscience* **41**, 163-183 (2018).

193. M. J. Redinbaugh *et al.*, Thalamus Modulates Consciousness via Layer-Specific Control of Cortex. *Neuron* 10.1016/j.neuron.2020.01.005 (2020).

194. N. J. Priebe, D. Ferster, Mechanisms underlying cross-orientation suppression in cat visual cortex. *Nat Neurosci* **9**, 552-561 (2006).

195. T. C. Freeman, S. Durand, D. C. Kiper, M. Carandini, Suppression without inhibition in visual cortex. *Neuron* **35**, 759-771 (2002).

196. M. V. Tsodyks, W. E. Skaggs, T. J. Sejnowski, B. L. McNaughton, Paradoxical effects of external modulation of inhibitory interneurons. *J Neurosci* **17**, 4382-4388 (1997).

Supplemental Information for Dynamic Normalization

David J. Heeger and Klavdia O. Zemlianova

Corresponding author: David J. Heeger
Email: david.heeger@nyu.edu

Table of contents

Detailed Methods **1**

Input drive: temporal prefilter *1*

Input drive: spatial RFs *2*

Input drive: RF size *3*

Recurrent drive *3*

Derivations **5**

Notation conventions *5*

Fixed point *5*

Effective gain *7*

Effective time constant *8*

Variants **9**

Bifurcation Analysis **14**

References **16**

Detailed Methods

Input drive: temporal prefilter

Simulated simple-cell responses $\mathbf{y}$ depended on an input drive $\mathbf{z}$, computed as a weighted sum of LGN inputs $\mathbf{x}$ (**Eq. 1**). LGN inputs were presumed to have two types of temporal impulse response functions (**Fig. S1a**), and each of the two temporal responses were paired with each of the various spatial receptive fields (RFs).

The temporal prefilter was a recursive quadrature temporal filter, that itself was based on ORGaNICs (1). For real-valued inputs:

$$\begin{aligned} &\tau_x \frac{dx}{dt} = -x + \lambda\left(x_0 + \mathrm{Im}\left(x\right)\right) + \left(1-\lambda\right)\hat{x} \ , \\ &\hat{x} = wx \ , \\ &w = 1 + i2\pi\tau\omega \ , \end{aligned} \tag{S1}$$

where $x_0(t)$ is the input and $x(t)$ is the filter output. The value of λ determines the effective time constant, and the value of ω determines the preferred temporal frequency. For complex-valued inputs:

$$\tau_x \frac{dx}{dt} = -x + \lambda x_0 + (1-\lambda)\hat{x} \ . \qquad \text{(S2)}$$

The temporal filter was cascaded, analogous to cascading a standard exponential lowpass filter. The response of the nth filter in the cascade was:

$$\begin{aligned} \tau_x \frac{dx_n}{dt} &= -x_n + \lambda x_{n-1} + (1-\lambda)\hat{x}_n \ , \\ \hat{x}_n &= w x_n \ , \\ w &= 1 + i 2\pi\tau_x \omega \ , \end{aligned} \qquad \text{(S3)}$$

for n=1 to N (i.e., x_N corresponds to the LGN responses). The response of the first filter in the cascade was:

$$\tau_x \frac{dx_1}{dt} = -x_1 + \lambda\left(x_0 + \mathrm{Im}(x_1)\right) + (1-\lambda)\hat{x}_1 \ , \qquad \text{(S4)}$$

where $x_0(t)$ was the input stimulus. The parameter values for the prefilters were: N=2; λ=0.04; τ_x=1 ms; ω=8 Hz. Consequently, the simulated LGN neurons had 2 temporal impulse response functions (**Fig. S1a**), with quadrature phases, matching the preferred temporal frequency of the simulated cortical neurons (ω=8 Hz).

Input drive: spatial RFs

Simulated simple-cell responses depended on a weighted sum of the LGN inputs. The rows of the encoding matrix $\mathbf{W}_{zx}$ in **Eq. 1** were the spatial RFs of the simple cells (**Figs. S1b**,**c**,**d**); $\mathbf{W}_{zx}$ was an NxM matrix of weights where N is the number of simple cells and M is the number of LGN inputs. The LGN inputs comprise pairs of ON- and OFF-center RFs (**Fig. 2**, center-surround weights), each halfwave rectified, and the input drive comprises differences between each such pair of LGN inputs (**Fig. 2**, solid and dashed blue lines), so that the input drive is a linear sum of the underlying (unrectified) LGN responses.

Spatial filters were based on the steerable pyramid, a subband image transform that decom-

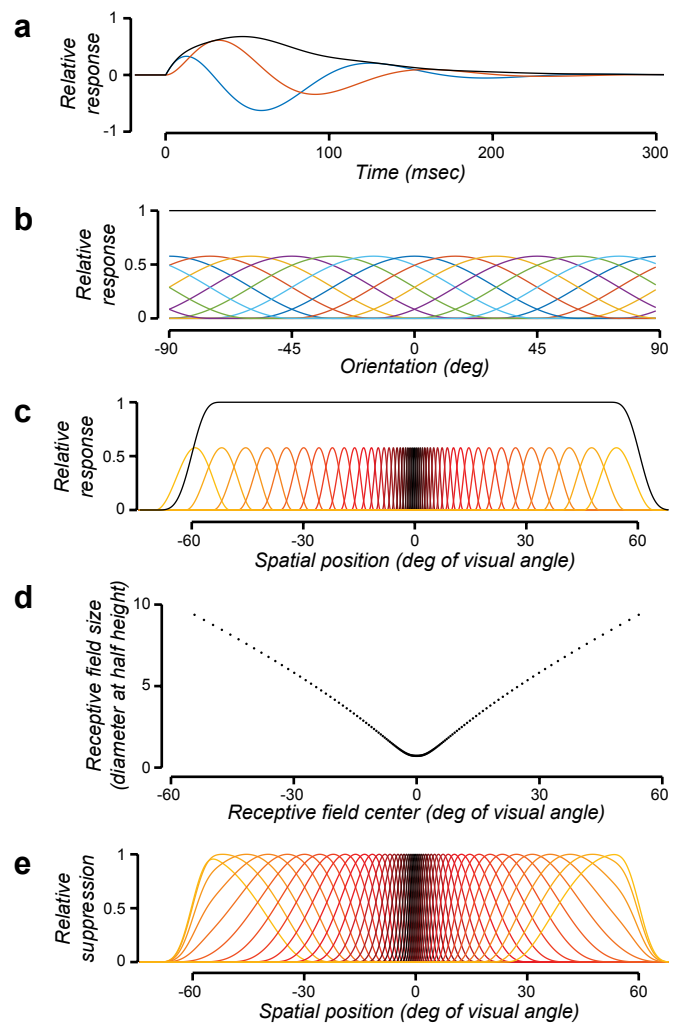

Figure S1. Temporal filters, receptive fields, and suppressive fields. a. Temporal filters. Blue and orange curves, recursive quadrature temporal filters. Black curve, amplitude (square-root of sum of squares) of the quadrature pair. **b.** Orientation tuning curves. Different colors correspond to different orientation preferences. Black curve, sum of squares of tuning curves. **c.** Receptive fields. Different colors correspond to different RF centers. Black curve, sum of squares of RFs. **d.** Receptive field size increases with eccentricity. **e.** Suppressive fields. Different curves correspond to different receptive fields. Each suppressive field (except those near ±60° eccentricity at the edge of the field of view) is about 4x larger than the corresponding receptive field.

poses an image into orientation and spatial frequency (SF) channels (2). The steerable pyramid simulated the responses of a large number of linear RFs, each of which computed a weighted sum of the stimulus image; the weights determined the orientation and SF tuning. The RFs were defined so that they covered all orientations, SFs, and spatial locations evenly, i.e., the sum of the squares was exactly equal to one (**Fig. S1b,c**). For each SF and orientation, there were 4 spatial phases and 2 temporal phases. For each orientation and SF, there were RFs with four different phases, like odd- and even-phase Gabor filters along with their anti-phase complements. Each of these 4 spatial phases were combined with each of the two temporal prefilters. The responses of these space-time separable linear filters provided the input drives to the population of simple cells. The end result was that V1 simple-cell responses behaved like spatiotemporal linear filters with various spatial RF locations, orientation preferences, and different temporal phases, that were half-squared (halfwave rectified and squared) (3) and normalized. The responses of a second population of direction-selective simple cells may be computed as a weighted sum of these space-time separable simple cells (4).

V1 complex-cell responses were simulated by summing the different temporal phases of the simple-cell responses. Because the response of each simple cell was half-squared, the sum computed what has been called an "energy" response (3, 4). The energy response depended on the local spectral energy within a spatial region of the stimulus, for a particular orientation and SF. Because the simple cell responses were normalized, the complex cells behaved like normalized, spatiotemporal energy filters.

Because the full set of SF and orientation channels was expensive to compute, the simulation results were instead computed using a reduced set of RFs. For **Figs. 3-4**, we simulated a collection of neurons with 12 different orientation orientation preferences, but all with the same SF preference and the same RF center. For **Figs. 5-6**, we simulated a collection of neurons with the same 12 orientation tuning curves, covering the horizontal meridian of the visual field from -60° to 60° eccentricity.

The orientation tuning curves for the RFs in the steerable pyramid are each one cycle of a raised cosine:

$$\begin{aligned} &\psi_j\left(\theta\right) \propto \tfrac{1}{2}\left(\cos\left(\tfrac{\pi}{60}\left(\theta-\theta_j\right)\right)+1\right) , \\ &\text{for } -\pi \le \tfrac{\pi}{60}\left(\theta-\theta_j\right) \le \pi, \text{ and } \psi_j\left(\theta\right)=0 \text{ otherwise,} \end{aligned} \qquad \text{(S5)}$$

where θ is stimulus orientation (in units of degrees), θ_j is the preferred preferred orientation of the jth neuron, ψ_j is the tuning curve, and the proportionality constant was chosen such that the sum of the squares of the tuning curves was equal to 1. This corresponds to an orientation bandwidth of 22° (half width at half height), given that firing rate responses were half-squared (**Eq. 1**, 2nd line).

Input drive: RF size

RF size increased with eccentricity (**Fig. S1d**), approximating measurements of V1 RF size and cortical magnification (5-9). Specifically, we warped visual space:

$$\xi' = \lambda\left|\xi\right|^{3.5} + \left(1-\lambda\right)\xi , \qquad \text{(S6)}$$

where $0 < \xi' < 1$ is the eccentricity in the visual field after warping and where $0 < \xi < 1$ is the eccentricity before warping. Both ξ and ξ' are each unit-less quantities, expressed as a proportion of the field of view. To convert to eccentricity in units of degrees of visual angle, we multiplied by the field of view, e.g., $60\,\xi$ was eccentricity in units of degrees of visual angle when the field of view was ±60° eccentricity.

Recurrent drive

Simulated simple-cell responses $\mathbf{y}$ also depended on a recurrent drive $\hat{\mathbf{y}}$, computed as a weighted sum of the square-root of the responses $\mathbf{y}$. The recurrent weight matrix $\mathbf{W}_{\hat{y}y}$ was an NxN matrix. An example of a simple cell's recurrent drive equals the difference between the square root of its own firing rate and the square root of the response of another simple cell with a complementary RF, i.e., with opposite ON- and OFF- subregions (**Fig. 2**, solid and dashed green lines). Simple cells with complementary RFs are adjacent to one another in V1 and they exhibit mutual inhibition (10). This difference reconstructs the underlying (unrectified) membrane potential fluctuations $\hat{y}_j = v_j$, such that the input drive z_j

is lowpass filtered by **Eq. 1** to yield the membrane potential v_j. The effective time constant of the lowpass filter depends on the intrinsic time constant τ_v and the modulator responses a_j.

An alternative for the recurrent weight matrix combines the responses of simple cells with all 4 temporal phases (anti-phase and quadrature phase). This elaborated recurrent drive acts as a bandpass filter on the input drive, with any desired preferred temporal frequency ω, and with a bandwidth that depends on the effective time constant of the circuit. Specifically:

$$\begin{aligned}
\hat{y}_{j.0} &= \left(\sqrt{y_{j,0}} - \sqrt{y_{j,180}}\right) - 2\pi\omega\tau_v\left(\sqrt{y_{j,90}} - \sqrt{y_{j,270}}\right) , \\
\hat{y}_{j.180} &= \left(\sqrt{y_{j,180}} - \sqrt{y_{j,0}}\right) - 2\pi\omega\tau_v\left(\sqrt{y_{j,270}} - \sqrt{y_{j,90}}\right) , \\
\hat{y}_{j.90} &= 2\pi\omega\tau_v\left(\sqrt{y_{j,0}} - \sqrt{y_{j,180}}\right) + \left(\sqrt{y_{j,90}} - \sqrt{y_{j,270}}\right) , \\
\hat{y}_{j.270} &= 2\pi\omega\tau_v\left(\sqrt{y_{j,180}} - \sqrt{y_{j,0}}\right) + \left(\sqrt{y_{j,270}} - \sqrt{y_{j,90}}\right) .
\end{aligned} \tag{S7}$$

The subscript φ in $\hat{y}_{j,\varphi}$ is the temporal phase of the simple cell responses. The recurrent drive given by **Eq. S7** is a temporal prediction over time of the simple cell responses (11, 12).

Derivations

Notation conventions

$\mathbf{x}^2$: element-by-element squaring

$\sqrt{\mathbf{x}}$: element-by-element positive square root

$\frac{\mathbf{x}}{\mathbf{y}}$: element-by-element division

$D(\mathbf{x})$: diagonal matrix with $\mathbf{x}$ along diagonal

$\mathbf{1}$: vector of 1's

$x^+ = \lfloor x \rfloor = \max(x,0)$

$x^- = \lfloor -x \rfloor = \max(-x,0)$

Fixed point

To derive the fixed point (**Eq. 4**) of the dynamical system given by **Eqs. 1-3**, we first rewrite the equations for the simple case in which the recurrent drive equals the difference between the square root of its own firing rate and the square root of the response of another simple cell with a complementary RF:

$$\tau_v \frac{dv_j}{dt} = -v_j + \left(\tfrac{b_0}{1+b_0}\right) z_j + \left(\tfrac{1}{1+a_j}\right)\left(\sqrt{y_j^+} - \sqrt{y_j^-}\right) ,$$

$$\tau_a \frac{da_j}{dt} = -a_j + \sqrt{u_j} + \sqrt{u_j}\, a_j ,$$

$$\tau_u \frac{du_j}{dt} = -u_j + \sum_k w_{jk} y_k u_k + \left(\tfrac{\sigma b_0}{1+b_0}\right)^2 ,$$

$$y_j^+ = \lfloor v_j \rfloor^2 \text{ and } y_j^- = \lfloor -v_j \rfloor^2 ,$$

$$\text{i.e., } v_j = \left(\sqrt{y_j^+} - \sqrt{y_j^-}\right) \text{ and } y_j = v_j^2 = y_j^+ + y_j^- , \qquad \text{(S8)}$$

$b_0 > 0$ is a constant,

w_{jk} are the elements of the normalization weight matrix $\mathbf{W}$,

the values of u_j are subject to the constraint that $u_{\min} \le u_j$

where $u_j = u_{\min} = \left(\frac{\sigma b_0}{1+b_0}\right)^2$ and $a_j = a_{\min} = \frac{\sigma b_0}{1+b_0-\sigma b_0} > 0$ when $\mathbf{y} = \mathbf{0}$.

Set the derivatives in **Eq. S8** equal to 0 and simplify:

$$\frac{d\mathbf{v}}{dt} = 0 :$$

$$v_j = \left(\tfrac{b_0}{1+b_0}\right) z_j + \left(\tfrac{1}{1+a_j}\right)\left(\sqrt{y_j^+} - \sqrt{y_j^-}\right) ,$$

$$v_j = \left(\tfrac{b_0}{1+b_0}\right) z_j + \left(\tfrac{1}{1+a_j}\right) v_j ,$$

$$\left(\tfrac{a_j}{1+a_j}\right) v_j = \left(\tfrac{b_0}{1+b_0}\right) z_j , \qquad \text{(S9)}$$

$$\left(\tfrac{a_j}{1+a_j}\right)^2 y_j = \left(\tfrac{b_0}{1+b_0}\right)^2 z_j^2 ,$$

$$y_j = \left(\tfrac{1+a_j}{a_j}\right)^2 \left(\tfrac{b_0}{1+b_0}\right)^2 z_j^2 ,$$

$$D(\mathbf{y})\left(\tfrac{\mathbf{a}}{1+\mathbf{a}}\right)^2 = \left(\tfrac{b_0}{1+b_0}\right)^2 \mathbf{z}^2 .$$

$$\frac{d\mathbf{u}}{dt} = 0 :$$

$$u_j = \sum_k w_{jk} y_k u_k + \left(\tfrac{\sigma b_0}{1+b_0}\right)^2 ,$$

$$\mathbf{u} = \mathbf{W} D(\mathbf{y}) \mathbf{u} + \left(\tfrac{\sigma b_0}{1+b_0}\right)^2 , \qquad \text{(S10)}$$

$$\left(\mathbf{I} - \mathbf{W} D(\mathbf{y})\right)\mathbf{u} = \left(\tfrac{\sigma b_0}{1+b_0}\right)^2 \mathbf{1} ,$$

$$\mathbf{u} = \left(\tfrac{\sigma b_0}{1+b_0}\right)^2 \left(\mathbf{I} - \mathbf{W} D(\mathbf{y})\right)^{-1} \mathbf{1} .$$

$$\frac{d\mathbf{a}}{dt} = 0 :$$

$$a_j = \sqrt{u_j} + \sqrt{u_j}\, a_j ,$$

$$a_j = \left(1 + a_j\right)\sqrt{u_j} , \qquad \text{(S11)}$$

$$\left(\tfrac{a_j}{1+a_j}\right)^2 = u_j ,$$

$$\left(\tfrac{\mathbf{a}}{1+\mathbf{a}}\right)^2 = \mathbf{u} .$$

Combine the last line of **Eq. S10** with the last line of **Eq. S11**:

$$
\begin{aligned}
&\left(\tfrac{\mathbf{a}}{1+\mathbf{a}}\right)^2 = \left(\tfrac{\sigma b_0}{1+b_0}\right)^2 \left(\mathbf{I} - \mathbf{W}D(\mathbf{y})\right)^{-1} \mathbf{1} \ , \\
&\left(\mathbf{I} - \mathbf{W}D(\mathbf{y})\right)\left(\tfrac{\mathbf{a}}{1+\mathbf{a}}\right)^2 = \left(\tfrac{\sigma b_0}{1+b_0}\right)^2 \mathbf{1} \ , \\
&\left(\mathbf{I} - \mathbf{W}D(\mathbf{y})\right)\left(\tfrac{\mathbf{a}}{1+\mathbf{a}}\right)^2 = \left(\tfrac{\sigma b_0}{1+b_0}\right)^2 D\left(\mathbf{y}\right)^{-1} \mathbf{y} \ , \\
&D\left(\mathbf{y}\right)\left(\mathbf{I} - \mathbf{W}D(\mathbf{y})\right)\left(\tfrac{\mathbf{a}}{1+\mathbf{a}}\right)^2 = \left(\tfrac{\sigma b_0}{1+b_0}\right)^2 \mathbf{y} \ , \\
&\left[D\left(\mathbf{y}\right) - D(\mathbf{y})\mathbf{W}D\left(\mathbf{y}\right)\right]\left(\tfrac{\mathbf{a}}{1+\mathbf{a}}\right)^2 = \left(\tfrac{\sigma b_0}{1+b_0}\right)^2 \mathbf{y} \ , \\
&\left(\mathbf{I} - D(\mathbf{y})\mathbf{W}\right) D\left(\mathbf{y}\right)\left(\tfrac{\mathbf{a}}{1+\mathbf{a}}\right)^2 = \left(\tfrac{\sigma b_0}{1+b_0}\right)^2 \mathbf{y} \ .
\end{aligned}
\tag{S12}
$$

Substitute from the last line of **Eq. S9** and simplify:

$$
\begin{aligned}
&\left(\tfrac{\sigma b_0}{1+b_0}\right)^2 \mathbf{y} = \left(\mathbf{I} - D(\mathbf{y})\mathbf{W}\right)\left(\tfrac{b_0}{1+b_0}\right)^2 \mathbf{z}^2 \ , \\
&\sigma^2 \mathbf{y} = \left(\mathbf{I} - D(\mathbf{y})\mathbf{W}\right)\mathbf{z}^2 \ , \\
&\sigma^2 \mathbf{y} = \mathbf{z}^2 - D(\mathbf{y})\mathbf{W}\mathbf{z}^2 \ , \\
&\sigma^2 \mathbf{y} = \mathbf{z}^2 - D(\mathbf{W}\mathbf{z}^2)\mathbf{y} \ , \\
&\sigma^2 \mathbf{y} + D(\mathbf{W}\mathbf{z}^2)\mathbf{y} = \mathbf{z}^2 \ , \\
&\left(\sigma^2 \mathbf{I} + D(\mathbf{W}\mathbf{z}^2)\right)\mathbf{y} = \mathbf{z}^2 \ , \\
&D\left(\sigma^2 + \mathbf{W}\mathbf{z}^2\right)\mathbf{y} = \mathbf{z}^2 \ , \\
&\mathbf{y} = \left(D\left(\sigma^2 + \mathbf{W}\mathbf{z}^2\right)\right)^{-1} \mathbf{z}^2 \ , \\
&\mathbf{y} = \frac{\mathbf{z}^2}{\sigma^2 + \mathbf{W}\mathbf{z}^2} \ .
\end{aligned}
\tag{S13}
$$

Effective gain

To derive the an expression for the effective gain, we begin with the last line of **Eq. S13**. The effective gain is the ratio of each element of $\mathbf{y}$ to each element of $\mathbf{z}^2$:

$$
\mathbf{g} = \frac{1}{\sigma^2 + \mathbf{W}\mathbf{z}^2} \ . \tag{S14}
$$

Because the normalization weights $\mathbf{W}$ are all positive:

$$
\mathbf{g} < g_{\max} \ \text{ where } g_{\max} = \tfrac{1}{\sigma^2} \ . \tag{S15}
$$

The expression for the effective gain (**Eq. S14**) simplifies for stimuli comprised of sinusoidal gratings, because the normalization weight matrix $\mathbf{W}$ was scaled such that the effective gain $g = 1$ for a full-contrast, full-field grating with a neuron's preferred spatiotemporal frequency and orientation. For a single sinusoidal grating $\mathbf{W}\mathbf{z}^2$ is proportional to the squared contrast c^2. For sums of gratings, $\mathbf{W}\mathbf{z}^2$ is proportional to a weighted sum of the squared contrasts (e.g., as expressed by **Eq. 6** for a test grating of preferred orientation restricted to the RF and a mask grating that by itself does not evoke a response).

Effective time constant

To derive an expression for effective time constant, we begin by rewriting the first line of **Eq. S8**:

$$\begin{aligned}
&\tau_v \frac{dv_j}{dt} = -v_j + \left(\tfrac{b_0}{1+b_0}\right) z_j + \left(\tfrac{1}{1+a_j}\right) v_j \ , \\
&\tau_v \frac{dv_j}{dt} = -\left(\tfrac{a_j}{1+a_j}\right) v_j + \left(\tfrac{b_0}{1+b_0}\right) z_j \ , \\
&\tau_j \frac{dv_j}{dt} = -v_j + \left(\tfrac{b_0}{1+b_0}\right)\left(\tfrac{1+a_j}{a_j}\right) z_j \ , \\
&\text{where } \tau_j = \left(\tfrac{1+a_j}{a_j}\right)\tau_v \ .
\end{aligned} \tag{S16}$$

Substitute from the last line of **Eq. S11**:

$$\tau = \frac{\tau_v}{\sqrt{\mathbf{u}}} \tag{S17}$$

To express the effective time constant in terms of the effective gain, we first derive another expression for the effective gain by combining the fixed point from **Eq. S9** with the last line of **Eq. S11**:

$$\begin{aligned}
&\mathbf{y} = \left(\tfrac{1+\mathbf{a}}{\mathbf{a}}\right)^2 \left(\tfrac{b_0}{1+b_0}\right)^2 \mathbf{z}^2 \ , \\
&\mathbf{g} = \left(\tfrac{1+\mathbf{a}}{\mathbf{a}}\right)^2 \left(\tfrac{b_0}{1+b_0}\right)^2 \ , \\
&\mathbf{g} = \left(\tfrac{1}{\mathbf{u}}\right)\left(\tfrac{b_0}{1+b_0}\right)^2 \ .
\end{aligned} \tag{S18}$$

I.e.,

$$\tfrac{1}{\sqrt{\mathbf{u}}} = \left(\tfrac{1+b_0}{b_0}\right)\sqrt{\mathbf{g}} \ . \tag{S19}$$

Combine **Eqs. S17** and **S19**:

$$\tau = \tau_v \left(\tfrac{1+b_0}{b_0}\right)\sqrt{\mathbf{g}} \tag{S20}$$

Variants

The circuit model expressed by **Eqs. 1-3** is but one example of a family of dynamical systems models of normalization, each of which implements normalization via recurrent amplification.

A simple variant of an ORGaNIC normalization circuit is expressed by the following coupled pair of neural integrators:

$$\begin{aligned} \tau_y \frac{dy_j}{dt} &= -y_j + b_0 z_j + \left(1 - a_j\right) y_j \ , \\ \tau_a \frac{da_j}{dt} &= -a_j + \sum_k w_{jk} y_k a_k + \sigma b_0 \ . \end{aligned} \tag{S21}$$

To derive the fixed point for this dynamical system, set the derivatives equal to 0 and simplify:

$$\begin{aligned} \frac{dy_j}{dt} = 0 &: \ a_j y_j = b_0 z_j \ , \\ \frac{da_j}{dt} = 0 &: \ a_j = \sum_k w_{jk} y_k a_k + \sigma b_0 \ . \end{aligned} \tag{S22}$$

Substitute the first line of **Eq. S22** into the second line of **Eq. S22**:

$$a_j = b_0 \left(\sum_k w_{jk} z_k + \sigma \right) . \tag{S23}$$

Substitute this back into the first line of **Eq. S22**:

$$\begin{aligned} b_0 \left(\sum_k w_{jk} z_k + \sigma \right) y_j &= b_0 z_j \ , \\ \left(\sum_k w_{jk} z_k + \sigma \right) y_j &= z_j \ , \\ y_j &= \frac{z_j}{\sigma + \sum_k w_{jk} z_k} \ . \end{aligned} \tag{S24}$$

There is, however, considerable empirical evidence that the firing rate responses of V1 neurons depend on the contrast energy of the stimulus, i.e., the square of the input drive (3, 13, 14). In addition, squaring offers theoretical advantages. First, responses depended on the local spectral energy (ignoring phase) in a local spatiotemporal window of the stimulus (3, 4). Second, the summed responses across the population of neurons tile all orientations, SFs, and spatial locations evenly (2), i.e., the sum of the squares is exactly equal to one (**Fig. S1b,c**).

Elaborating **Eq. S21** with halfwave rectification and squaring yields another variant:

$$\begin{aligned} \tau_v \frac{dv_j}{dt} &= -v_j + b_0 z_j + \left(1 - \sqrt{a_j}\right)\left(\sqrt{y_j^+} - \sqrt{y_j^-}\right) \ , \\ \tau_a \frac{da_j}{dt} &= -a_j + \sum_k w_{jk} y_k a_k + \sigma^2 b_0^2 \ . \end{aligned} \tag{S25}$$

This variant has the same fixed point as **Eqs. 1-3** (equivalently **Eq. S8**); the derivation of the fixed point for this system is very similar to that shown above for **Eq. S8**. This circuit exhibits different dynamics from **Eqs. 1-3** even though they both share the same fixed point (see below, *Bifurcation Analysis*).

Another variant is:

$$\begin{aligned}
\tau_v \frac{dv_j}{dt} &= -v_j + \left(\tfrac{b_0}{1+b_0}\right) z_j + \left(\tfrac{2a_j}{1+a_j}\right)\left(\sqrt{y_j^+} - \sqrt{y_j^-}\right) , \\
\tau_a \frac{da_j}{dt} &= -a_j - \sqrt{u_j} - \sqrt{u_j}\, a_j + d , \\
\tau_u \frac{du_j}{dt} &= -u_j + \sum_k w_{jk} y_k u_k + \left(\tfrac{\sigma b_0}{1+b_0}\right)^2 ,
\end{aligned} \tag{S26}$$

where $d > 0$. In this variant, we replaced $1/(1+\mathbf{a})$ in **Eq. 1** with $2\mathbf{a}/(1+\mathbf{a})$, in which $0<\mathbf{a}<1$, with concomitant changes to the equation for $\mathbf{a}$ (**Eq. 2**). When the value of $d = 1$, the fixed point for this system is the same as that for **Eqs. 1-3** (the derivation follows that shown above for **Eqs. 1-3**). The dynamics are also similar (the two systems are related by a simple change of variables). But when $d < 1$, the gain of this system is reduced.

To derive the gain as a function of d, consider the reduced system in which each of the variables is a scalar instead of a vector (i.e., there's only neuron of each type instead of population of neurons with different RFs, SF preferences, and orientation preferences):

$$\begin{aligned}
\tau_v \frac{dv}{dt} &= -v + \left(\tfrac{b_0}{1+b_0}\right) z + \left(\tfrac{2a}{1+a}\right)\sqrt{y} , \\
\tau_a \frac{da}{dt} &= -a - \sqrt{u} - \sqrt{u}\, a + d , \\
\tau_u \frac{du}{dt} &= -u + yu + \left(\tfrac{\sigma b_0}{1+b_0}\right)^2 , \\
z &\geq 0 .
\end{aligned} \tag{S27}$$

The fixed point for this system is derived, again, by setting the derivatives equal to zero:

$$\begin{aligned}
&\frac{dv}{dt} = 0 : \\
&v = \left(\tfrac{b_0}{1+b_0}\right) z + \left(\tfrac{2a}{1+a}\right) v , \\
&\left(\tfrac{1-a}{1+a}\right) v = \left(\tfrac{b_0}{1+b_0}\right) z , \\
&\left(\tfrac{1-a}{1+a}\right)^2 y = \left(\tfrac{b_0}{1+b_0}\right)^2 z^2 , \\
&y = \left(\tfrac{1+a}{1-a}\right)^2 \left(\tfrac{b_0}{1+b_0}\right)^2 z^2 .
\end{aligned} \tag{S28}$$

$$\begin{aligned}
&\frac{du}{dt} = 0 : \\
&u = yu + \left(\tfrac{\sigma b_0}{1+b_0}\right)^2 , \\
&u(1-y) = \left(\tfrac{\sigma b_0}{1+b_0}\right)^2 , \\
&u = \left(\tfrac{\sigma b_0}{1+b_0}\right)^2 \frac{1}{(1-y)} .
\end{aligned} \tag{S29}$$

$$\frac{da}{dt}=0:$$
$$\left(d-a\right)=\sqrt{u}+\sqrt{u}a\ ,$$
$$\left(d-a\right)=\left(1+a\right)\sqrt{u}\ ,$$
$$u=\left(\tfrac{d-a}{1+a}\right)^2\ . \tag{S30}$$

Combine the last line of **Eq. S29** with the last line of **Eq. S30**:

$$\left(\tfrac{1+a}{d-a}\right)^2=\left(\tfrac{1+b_0}{\sigma b_0}\right)^2\left(1-y\right)\ . \tag{S31}$$

Combine the last line of **Eq. S28** with **Eq. S31**:

$$y=\left(\tfrac{1+a}{1-a}\right)^2\left(\tfrac{b_0}{1+b_0}\right)^2 z^2\ ,$$
$$y=\left(\tfrac{d-a}{1-a}\right)^2\left(\tfrac{1+a}{d-a}\right)^2\left(\tfrac{b_0}{1+b_0}\right)^2 z^2\ ,$$
$$y=\left(\tfrac{d-a}{1-a}\right)^2\left(1-y\right)\left(\tfrac{1+b_0}{\sigma b_0}\right)^2\left(\tfrac{b_0}{1+b_0}\right)^2 z^2\ , \tag{S32}$$
$$\sigma^2 y=\left(\tfrac{d-a}{1-a}\right)^2\left(1-y\right)z^2\ .$$

Simplify:

$$\sigma^2 y=\left(\tfrac{d-a}{1-a}\right)^2\left(z^2-z^2 y\right)\ ,$$
$$y\left(\sigma^2+\left(\tfrac{d-a}{1-a}\right)^2 z^2\right)=\left(\tfrac{d-a}{1-a}\right)^2 z^2\ ,$$
$$y=\frac{\left(\tfrac{d-a}{1-a}\right)^2 z^2}{\sigma^2+\left(\tfrac{d-a}{1-a}\right)^2 z^2}\ , \tag{S33}$$
$$y=\frac{z^2}{\left(\sigma'\right)^2+z^2}\ ,$$
$$\text{where } \left(\sigma'\right)=\left(\tfrac{1-a}{d-a}\right)\sigma\ .$$

For $d<1$, $\sigma'>\sigma$ and the effective gain is reduced.

Some of the other variants are as follows. Each is written as reduced systems in which each of the variables is a scalar instead of a vector, although each can also be expressed as a full population with arbitrary (non-negative normalization weights).

$$\tau_y\frac{dy}{dt}=-y+b_0 z+\left(1-a\right)y\ ,$$
$$\tau_a\frac{da}{dt}=-a+ya+\sigma b_0\ , \tag{S34}$$
$$z\geq 0\ .$$

$$\begin{aligned}
&\tau_v \frac{dv}{dt} = -v + b_0 z + \left(1-\sqrt{a}\right)\sqrt{y} \ , \\
&\tau_a \frac{da}{dt} = -a + ya + \sigma^2 b_0^2 \ , \\
&y = v^2 \ , \\
&z \geq 0 \ .
\end{aligned} \tag{S35}$$

$$\begin{aligned}
&\tau_v \frac{dv}{dt} = -v + b_0 z + \left(1-a\right)\sqrt{y} \ , \\
&\tau_a \frac{da}{dt} = -a + \sqrt{u} \ , \\
&\tau_u \frac{du}{dt} = -u + yu + \sigma^2 b_0^2 \ , \\
&y = v^2 \ , \\
&z \geq 0 \ .
\end{aligned} \tag{S36}$$

$$\begin{aligned}
&\tau_v \frac{dv}{dt} = -v + \left(\tfrac{b_0}{1+b_0}\right) z + \left(\tfrac{1}{1+a}\right)\sqrt{y} \ , \\
&\tau_a \frac{da}{dt} = -a + \sqrt{u} + \sqrt{u}a \ , \\
&\tau_u \frac{du}{dt} = -u + yu + \left(\tfrac{\sigma b_0}{1+b_0}\right)^2 \ , \\
&y = v^2 \ , \\
&z \geq 0 \ .
\end{aligned} \tag{S37}$$

$$\begin{aligned}
&\tau_v \frac{dv}{dt} = -v + \left(\tfrac{1}{1+b_0}\right) z + \left(\tfrac{1}{1+a}\right)\sqrt{y} \ , \\
&\tau_a \frac{da}{dt} = -a + \sqrt{u} + \sqrt{u}a \ , \\
&\tau_u \frac{du}{dt} = -u + yu + \left(\tfrac{\sigma}{1+b_0}\right)^2 \ , \\
&y = v^2 \ , \\
&z \geq 0 \ .
\end{aligned} \tag{S38}$$

$$
\begin{aligned}
&\tau_v \frac{dv}{dt} = -v + \left(\tfrac{b_0}{1+b_0}\right) z + \left(\tfrac{1}{1+a}\right)\sqrt{y} \ , \\
&\tau_a \frac{da}{dt} = -a + u_1 + u_1 a \ , \\
&\tau_{u_1} \frac{du_1}{dt} = -u_1 + \frac{u_2}{u_1} \text{ such that } u_1 > 0 \ , \\
&\tau_{u_2} \frac{du_2}{dt} = -u_2 + y u_2 + \left(\tfrac{\sigma b_0}{1+b_0}\right)^2 \ , \\
&y = v^2 \ , \\
&z \geq 0 \ .
\end{aligned}
\tag{S39}
$$

Eqs. S35-S39 have the same fixed point. The fixed point for **Eq. 34** is similar, but without the squaring. **Eqs. S36-S39** exhibit the same or similar dynamics. **Eqs. S34-S35** exhibit different dynamics (see below, *Bifurcation Analysis*). **Eq. S34** is the reduced version of **Eq. S21**, **Eq. S35** is the reduced version of **Eq. S25**, and **Eq. S37** is the reduced version of **Eqs. 1-3** (equivalently **Eq. S8**). **Eq. S39** eliminates the square root in the expression for u; the square root of y may be eliminated analogously.

Bifurcation Analysis

The 2D bifurcation diagrams in **Fig. 7e** were computed as follows, based on the reduced model (**Eq. S37**). The fixed points of that system of equations correspond to where all of the derivatives ($\mathrm{d}v/\mathrm{d}t$, $\mathrm{d}a/\mathrm{d}t$, and $\mathrm{d}u/\mathrm{d}t$) are equal to zero:

$$\begin{aligned} v &= \frac{z}{\sqrt{\sigma^2+z^2}} \ , \\ a &= \frac{\sqrt{u}}{1-\sqrt{u}} \ , \\ u &= \left(\frac{b_0}{1+b_0}\right)^2 \left(\sigma^2+z^2\right) \ . \end{aligned} \tag{S40}$$

There was a different fixed point for each value of the input drive z. The Jacobian of **Eq. S37** was analyzed to determine if a fixed point is stable (an attractor; **Fig. 7a**, solid curve) or unstable (typically associated with a limit cycle; **Fig. 7a**, dashed curve). The Jacobian is a 3x3 matrix of partial derivatives of **Eq. S37** evaluated at the fixed point:

$$\mathbf{J} = \begin{pmatrix} \frac{-1+\sqrt{u}}{\tau_a} & 0 & \frac{1+a}{2\tau_a\sqrt{u}} \\ \frac{-v}{\tau_v(1+a)^2} & \frac{-a}{\tau_v(1+a)} & 0 \\ 0 & \frac{2uv}{\tau_u} & \frac{v^2-1}{\tau_u} \end{pmatrix} \tag{S41}$$

To compute the Jacobian, the derivatives must be continuous, which is the case for our system of equations when a, v, and $u > 0$, which is the regime that we care about. Stability depends on the eigenvalues of this Jacobian matrix. If the real parts of all of the eigenvalues are negative, then the fixed point is stable. If at least one eigenvalue has a positive real part, then the fixed point is unstable because this means that there is at least one direction along which a trajectory will not return back to the fixed point. The intuition is like dropping a marble on a paraboloid. If the paraboloid is concave upward (like a bowl) then the marble will roll back to the fixed point at the bottom of the bowl. If it is concave downward (like an upside down bowl) or a hyperbolic paraboloid (a saddle), then there is at least one direction in which the marble will roll downward away from the fixed point.

A Hopf bifurcation occurs when a spiraling fixed point changes from stable to unstable (or vice versa), i.e., when the real part of a complex-conjugate pair of eigenvalues changes sign. The point at which the real part of the complex-valued eigenvalues is equal to zero is the Hopf bifurcation point. Requiring that the real part of the eigenvalues equal zero is equivalent to requiring a particular set of constraints on the determinant and trace of the Jacobian matrix (15), although we omit writing the exact set of constraints here as they are cumbersome. We found the points that satisfy these constraints by solving a polynomial in our six parameters: z, σ, b_0, τ_v, τ_a, and τ_u. Since we have a high dimensional parameter space, finding the roots of this polynomial is itself a hard problem. We therefore restricted our analysis to a subset of the parameter space by keeping σ and b_0 fixed and characterizing 3D slices through the other parameters, either (z, τ_v, τ_a) or (z, τ_a, τ_u). The condition on the eigenvalues to change sign alone is not sufficient to guarantee the existence of a limit cycle, although one almost always does arise (16). We therefore checked that a limit cycle did indeed arise (for each fixed point) using AUTO-07p (Version 0.8), a bifurcation analysis software platform for ordinary differential equations (17). Finally, we computed the frequencies of the observed oscillations (when a limit cycle appeared) using AUTO-07p. The oscillation frequencies for each panel of **Fig. 7e** were computed at a grid of values for z and τ_u.

A case of particularly interesting dynamics corresponds to the parameter regime given by b_0=5, τ_a=2, and τ_u=1. For these parameter values, and for increasing values of the input drive z, we found a periodic solution (i.e., a limit cycle) extending past the point where the Hopf bifurcation occurs. What this means is that there are two stable attractors in this regime, both a stable fixed point and a stable limit cycle, i.e., both convergence to steady state and oscillations. These two steady state behaviors exist simultaneously and the initial values of v, a, and u determine which of the two behaviors will be

observed.

We proved that the alternative 2-dimensional circuit, given by **Eq. S35**, does not exhibit oscillations. The fixed points of that system of equations correspond to where the derivatives ($\mathrm{d}v/\mathrm{d}t$ and $\mathrm{d}a/\mathrm{d}t$) are equal to zero:

$$v = \frac{z}{\sqrt{\sigma^2+z^2}} \ , \qquad a = b_0^2\left(\sigma^2+z^2\right) \ . \tag{S42}$$

These two equations are continuously differentiable, so we derived an expression for the eigenvalues of the Jacobian at the fixed point. The Jacobian is given by:

$$\mathbf{J} = \begin{pmatrix} \frac{-\sqrt{a}}{\tau_v} & \frac{-v}{2\tau_v\sqrt{a}} \\ \frac{2va}{\tau_a} & \frac{v^2-1}{\tau_a} \end{pmatrix} \tag{S43}$$

The eigenvalues are computed by solving the characteristic equation:

$$\det\left(\mathbf{J}-\lambda\mathbf{I}\right) = \left(\frac{\sqrt{a}}{\tau_v}-\lambda\right)\left(\frac{v^2-1}{\tau_a}-\lambda\right)+\frac{v^2\sqrt{a}}{\tau_a\tau_v} \tag{S44}$$

Solving for λ gives:

$$\lambda_{1,2} = \frac{1}{2}\left(\left(\frac{v^2-1}{\tau_a}-\frac{\sqrt{a}}{\tau_v}\right)\pm\sqrt{\left(\frac{v^2-1}{\tau_a}-\frac{\sqrt{a}}{\tau_v}\right)^2-\frac{4\sqrt{a}}{\tau_v\tau_a}}\right) \ . \tag{S45}$$

For a hopf bifurcation, the real part of this complex-conjugate pair of eigenvalues must be zero with non-zero imaginary part. However, this would require:

$$\left(\frac{v^2-1}{\tau_a}-\frac{\sqrt{a}}{\tau_v}\right) = 0 \ . \tag{S46}$$

But, in fact, the expression in **Eq. S46** (same as the first term in **Eq. S45**) is strictly less than zero because $v<1$, and τ_v, τ_a, and $a>0$. So this system will never change its stability. To determine the type of stability that the system exhibits we just need to determine the sign of the real parts of the eigenvalues. The expression under the square root in **Eq. S45** is smaller than the first term in **Eq. S45**, and we have already determined that the first term in **Eq. S45** is less than zero. Consequently, the real parts of the eigenvalues are negative, the fixed point is stable, and all of the trajectories approach the fixed point as $t\rightarrow\infty$.

References

1. D. J. Heeger, W. E. Mackey, Oscillatory recurrent gated neural integrator circuits (ORGaNICs), a unifying theoretical framework for neural dynamics. *Proc Natl Acad Sci U S A* **116**, 22783-22794 (2019).
2. E. P. Simoncelli, W. T. Freeman, E. H. Adelson, D. J. Heeger, Shiftable multi-scale transforms. *IEEE Transactions on Information Theory, Special Issue on Wavelets* **38**, 587-607 (1992).
3. D. J. Heeger, Half-squaring in responses of cat striate cells. *Vis Neurosci* **9**, 427-443 (1992).
4. E. H. Adelson, J. R. Bergen, Spatiotemporal energy models for the perception of motion. *Journal of the Optical Society of America A* **2**, 284-299 (1985).
5. J. C. Horton, W. F. Hoyt, The representation of the visual field in human striate cortex. *Archives of Ophthalmology* **109**, 816-824 (1991).
6. S. O. Dumoulin, B. A. Wandell, Population receptive field estimates in human visual cortex. *NeuroImage* **39**, 647-660 (2008).
7. J. Winawer, H. Horiguchi, R. A. Sayres, K. Amano, B. A. Wandell, Mapping hV4 and ventral occipital cortex: the venous eclipse. *J Vis* **10**, 1 (2010).
8. J. Freeman, E. P. Simoncelli, Metamers of the ventral stream. *Nat Neurosci* **14**, 1195-1201 (2011).
9. K. N. Kay, J. Winawer, A. Mezer, B. A. Wandell, Compressive spatial summation in human visual cortex. *J Neurophysiol* **110**, 481-494 (2013).
10. Z. Liu, J. P. Gaska, L. D. Jacobson, D. A. Pollen, Interneuronal interaction between members of quadrature phase and anti-phase pairs in the cat's visual cortex. *Vision Res* **32**, 1193-1198 (1992).
11. D. J. Heeger, Theory of cortical function. *Proc Natl Acad Sci U S A* **114**, 1773-1782 (2017).
12. D. J. Heeger, W. E. Mackey, ORGaNICs: A Theory of Working Memory in Brains and Machines. *arXiv preprint arXiv:1803.06288* (2018).
13. M. Carandini, D. J. Heeger, J. A. Movshon, Linearity and normalization in simple cells of the macaque primary visual cortex. *J Neurosci* **17**, 8621-8644 (1997).
14. W. S. Geisler, D. G. Albrecht, Visual cortex neurons in monkeys and cats: detection, discrimination, and identification. *Vis Neurosci* **14**, 897-919 (1997).
15. S. B.-D. Desmarchelier, A simple method to study local bifurcations of three and four-dimensional systems: characterizations and economic applications. (2017).
16. J. Guckenheimer, P. Holmes, "Local bifurcations" in Nonlinear oscillations, dynamical systems, and bifurcations of vector fields. (Springer, 1983), pp. 117-165.
17. E. Doedel, P. Kamthan (2007) AUTO-07p: Continuation and bifurcation software for ordinary differential equations. (Concordia University, Montreal).